Simulation of the Geometrically Exact Nonlinear String via Energy Quadratisation

Michele Ducceschi[a], Stefan Bilbao[b]

[a]*Department of Engineering, University of Bologna, IT*
[b]*Acoustics and Audio Group/Reid School of Music, Alison House, University of Edinburgh, UK*

Abstract

String vibration represents an active field of research in acoustics. Small-amplitude vibration is often assumed, leading to simplified physical models that can be simulated efficiently. However, the inclusion of nonlinear phenomena due to larger string stretchings is necessary to capture important features, and efficient numerical algorithms are currently lacking in this context. Of the available techniques, many lead to schemes which may only be solved iteratively, resulting in high computational cost, and the additional concerns of existence and uniqueness of solutions. Slow and fast waves are present concurrently in the transverse and longitudinal directions of motion, adding further complications concerning numerical dispersion. This work presents a linearly-implicit scheme for the simulation of the geometrically exact nonlinear string model. The scheme conserves a numerical energy, expressed as the sum of quadratic terms only, and including an auxiliary state variable yielding the nonlinear effects. This scheme allows to treat the transverse and longitudinal waves separately, using a mixed finite difference/modal scheme for the two directions of motion. A matrix decomposition algorithm is presented, so to treat the sparse and full parts of the update matrix separately. Numerical experiments are presented throughout.

Keywords: Energy Methods, Nonlinear Dynamics, Musical Acoustics, String Vibration, Invariant Energy Quadratisation

1. Introduction

The vibration of a musical string, to a first approximation, can be considered linear. From a numerical standpoint, the problem of linear string

vibration was explored in many works, see e.g., Ruiz [1, 2], Bacon and Bowsher [3], Chaigne and Askenfelt [4], Bensa *et. al* [5], Ducasse [6], and others.

Nonlinear behaviour results for moderate and high amplitudes of motion, and various physical models are available. One of the simplest such models includes tension-modulation effects, as per the Kirchhoff-Carrier model [7]. Numerically, this was approached using finite difference schemes [8] (Chapter 8) as well as Volterra series [9]. Longitudinal motion is neglected in this model, which was shown to be inaccurate, since an energy transfer always exists from the transverse to the longitudinal waves [10, 11].

Finer models, comprising longitudinal motion, can be obtained via geometric arguments. Here, one considers the strain of of a stretched string, and applies Hooke's law. Approximating the energy in a power series results in a model as per Morse and Ingard's [12] (Section 14.3). Numerically, this approximate model was solved via finite difference schemes [13, 8, 14], as well as modal methods, though with further simplifications on the coupling mechanism [15].

In the Morse and Ingard model, the hypothesis of weak linear degenerancy, as explained in [16], is not fulfilled, and this has lead researchers to study the the geometrically exact model. The finite element method, in particular, is preeminent here, see e.g. [17, 18, 19]. In [17, 18], the conservation of a non-negative numerical energy allows to derive a stability condition involving the mesh size and the time step. Since these methods are fully-implicit, they require the solution of a large nonlinear algebraic system at each time step, for which existence and uniqueness of the solution must be proven, and which are only approachable using iterative routines such as Newton-Raphson [20]. Further complications arise in the choice of the tolerance thresholds and maximum number of iterations of the routine.

For these reasons, in this work, a method is presented, such that the resulting numerical scheme is linearly-implicit in character, thus sidestepping the machinery of iterative methods. Here, existence and uniqueneness of the numerical update are proven by simple inspection of the update matrix, and efficiency is also greatly improved, since the update requires the solution of a single linear system. This particular form is obtained after quadratisation of the nonlinear potential, in a way that is analogous to the Invariant Energy Quadratisation method, proposed orginally for parabolic phase-field models [21, 22, 23].

Furthermore, wideband numerical dispersion reduction is achieved using a free parameter. Rather than increasing the formal order of accuracy, the

free parameter is used to increase the spectral accuracy across the whole frequency axis.

The article is structured as follows. In Section 2 the geometrically nonlinear string is discussed, including stiffness effects. A semi-discrete formulation is given in Section 3. The fully-discrete numerical scheme is detailed in Section 4, including a proof of conservation of the numerical energy. Section 5 details the LU factorisation employed to solve the associated linear system, and includes a computational test highlighting the speedups of the current formulation against previously available schemes. Section 6 details a method to reduce numerical dispersion in the transverse direction across a wideband portion of the frequency axis, using a free parameter for which an analytic expression is given. In Section 7, an application comprising the nonlinear string with source and loss terms is illustrated, highligting the passage from linear to fully nonlinear regimes. It is shown that very good results can be obtained using small oversampling factors compared to audio rate.

2. Nonlinear Wave Equation

The case of a nonlinear wave equation describing geometric nonlinearities in stiff strings will be considered here. The geometrically exact nonlinear potential has been used in previous works to simulate the behaviour of musical strings undergoing large amplitude vibration, and comprising a coupling between the longitudinal and transverse components of motion [17, 24, 19]. In the lossless, zero-input case, the system considered here is

$$\left(\rho A \partial_t^2 - T_0 \partial_x^2 + EI \partial_x^4\right) u(t,x) = \partial_x \left(\frac{\partial \phi}{\partial(\partial_x u)} \right), \tag{1a}$$

$$\left(\rho A \partial_t^2 - T_0 \partial_x^2\right) v(t,x) = \partial_x \left(\frac{\partial \phi}{\partial(\partial_x v)} \right), \tag{1b}$$

where

$$\phi = \phi(\partial_x u, \partial_x v) = \frac{EA - T_0}{2} \left(\sqrt{(1+\partial_x v)^2 + (\partial_x u)^2} - 1 \right)^2. \tag{2}$$

First, in (1) and in the following, the symbol ∂_j^i denotes a partial derivative along j of order i. The displacements are $u(t,x) : \mathbb{R}_0^+ \times [0,L] \to \mathbb{R}$ in the vertical or flexural direction (perpendicular to the string length), and $v(t,x) : \mathbb{R}_0^+ \times [0,L] \to \mathbb{R}$ in the longitudinal direction (parallel to the string length).

Constants appear as: volume density ρ, area of the cross section A ($= \pi r^2$ for a circular cross section of radius r), Young's modulus E, applied tension T_0, string length L, area moment of inertia I ($= \pi r^4/4$ for a circular cross section). Model (1) is geometrically exact [12, 17], and includes a stiffness term as per the Euler-Bernoulli beam model [25, 26]. Equations (1) must be completed by suitable initial conditions, assumed here differentiable, expressed as

$$u(0,x) = u_0(x),\ v(0,x) = v_0(x),\ \partial_t u(0,x) = p_0(x),\ \partial_t v(0,x) = q_0(x). \tag{3}$$

The nonlinear potential ϕ, as per (2), is non-negative when $EA \geq T_0$ (a condition that is always satisfied for musical strings). This condition will be assumed valid in the remainder. It is noted that the equations of motion for the geometrically exact nonlinear string are usually expressed in a different form (see e.g. [17, 19]), employing an expression of the potential energy which is non-negative in all cases, though yielding equations identical to (1). The form proposed here, in contrast to the usual form, allows to isolate linear terms proportional to T_0, as can be seen in both (1a) and (1b). This design choice is justified in a musical context, where strings operate in a regime driven by the flexural tension term. Here, the linear part of (1a) is unaffected by ϕ. Ultimately, this allows to achieve full audio bandwidth using reference sample rates, as will be shown in Section 6.

2.1. Energy Identities

For two square-integrable functions $f,\ g : [0, L] \to \mathbb{R}$ one may define an inner product and associated norm as

$$\langle f, g \rangle = \int_0^L f g \,\mathrm{d}x, \qquad \|f\| = \sqrt{\langle f, f \rangle}. \tag{4}$$

These definitions can be used to derive suitable energy identities for the nonlinear wave equation. Here, one takes an inner product of (1a) with $\partial_t u$, and of (1b) with $\partial_t v$, to get

$$\rho A \left\langle \partial_t u, \partial_t^2 u \right\rangle = T_0 \left\langle \partial_t u, \partial_x^2 u \right\rangle - EI \left\langle \partial_t u, \partial_x^4 u \right\rangle + \left\langle \partial_t u, \partial_x \left(\frac{\partial \phi}{\partial(\partial_x u)} \right) \right\rangle, \tag{5a}$$

$$\rho A \left\langle \partial_t v, \partial_t^2 v \right\rangle = T_0 \left\langle \partial_t v, \partial_x^2 v \right\rangle + \left\langle \partial_t v, \partial_x \left(\frac{\partial \phi}{\partial(\partial_x v)} \right) \right\rangle. \tag{5b}$$

Summing the two equations, after appropriate integration by parts, and using the fact that

$$\frac{d\phi}{dt} = \partial_t\partial_x u \left(\frac{\partial \phi}{\partial(\partial_x u)} \right) + \partial_t\partial_x v \left(\frac{\partial \phi}{\partial(\partial_x v)} \right), \tag{6}$$

one gets the following energy balance

$$\frac{dH}{dt} = \left(\langle \partial_t u, F_u \rangle - \langle \partial_t\partial_x u, M_u \rangle + \langle \partial_t v, F_v \rangle \right) \Big|_0^L, \tag{7}$$

where the boundary forces and moment, due to linear and nonlinear effects, are expressed as

$$F_u = T_0\partial_x u - EI\partial_x^3 u + \frac{\partial \phi}{\partial(\partial_x u)}, \;\; F_v = T_0\partial_x v + \frac{\partial \phi}{\partial(\partial_x v)}, \;\; M_u = -EI\partial_x^2 u.$$

The total energy is the sum of kinetic, linear and nonlinear potential energies, as

$$H(t) = E_k(t) + E_{pl}(t) + E_{pnl}(t), \tag{8}$$

where

$$E_k = \frac{\rho A}{2} \left(\|\partial_t u\|^2 + \|\partial_t v\|^2 \right), \tag{9a}$$

$$E_{pl} = \frac{T_0}{2} \left(\|\partial_x u\|^2 + \|\partial_x v\|^2 \right) + \frac{EI}{2} \left\|\partial_x^2 u\right\|^2, \tag{9b}$$

$$E_{pnl} = \left\| \sqrt{\phi} \right\|^2. \tag{9c}$$

which is non-negative. The right hand side of (7) consists of boundary terms. In order for the system to be conservative, it is sufficient to impose conditions such that the boundary terms vanish. Various combinations are possible, and one must be wary of the nonlinear terms when imposing the vanishing of the forces at the boundary. Here, the string is assumed to be simply-supported flexurally, and fixed longitudinally, i.e.

$$u = \partial_x^2 u = v = 0 \text{ at } x = 0, L \tag{10}$$

When these conditions are enforced, energy conservation holds, and thus

$$H(t) = H(0) \triangleq H_0. \tag{11}$$

An expression for H_0 is derived by direct subsitution of (3) (plus appropriate derivatives) into (9). Bounds on solution growth may be expressed easily from such conserved energy, as

$$0 \leq \|\partial_t u\| \leq \sqrt{2H_0/\rho A}, \quad 0 \leq \|\partial_x u\| \leq \sqrt{2H_0/T_0}, \tag{12}$$

with analogous bounds holding for the longitudinal term. Since the string is fixed at both ends, bounds on u, rather than its derivatives, may be obtained here, see e.g. [8] (Chapter 6) and [17].

2.2. Quadratisation

In view of the numerical application presented below, the nonlinear potential energy is now quadratised by means of the function $\psi : \mathbb{R}^2 \to \mathbb{R}_0^+$ defined as

$$\psi(\partial_x u, \partial_x v) = \sqrt{2\phi(\partial_x u, \partial_x v)}. \tag{13}$$

Under such transformation, the total energy is

$$H(t) = E_k(t) + E_{pl}(t) + E_{pnl}(t), \tag{14}$$

where E_k, E_{pl} are the same as (9), but where

$$E_{pnl} = \frac{\|\psi\|^2}{2}, \tag{15}$$

The total energy here includes only quadratic terms, and the equations of motion read

$$\left(\rho A\partial_t^2 - T_0\partial_x^2 + EI\partial_x^4\right) u(t,x) = \partial_x \left(g_u \psi\right), \tag{16a}$$

$$\left(\rho A\partial_t^2 - T_0\partial_x^2\right) v(t,x) = \partial_x \left(g_v \psi\right), \tag{16b}$$

$$\frac{d\psi}{dt} = g_u \partial_t \partial_x u + g_v \partial_t \partial_x v. \tag{16c}$$

These are completed by the identities

$$g_u = \frac{\partial \psi}{\partial(\partial_x u)}, \quad g_v = \frac{\partial \psi}{\partial(\partial_x v)}. \tag{17}$$

The transformation (13) forms the core of the Invariant Energy Quadratisation method (IEQ), proposed by Yang and associates in the context of nonlinear parabolic phase-field models [21, 22, 23], and allowing for a linearly-implicit formulation of the associated numerical schemes. In parallel, a

different kind of quadratisation was proposed by Hélie, Lopes and Falaize within the context of Port-Hamiltonian systems [27, 28, 29, 30]. The former method, IEQ, may be applied to any non-negative multivariate potential ϕ. For the latter method, further requirements on convexity must be met by the function ϕ [30], precluding the possibility of treating various cases such as e.g. non-invertible potentials. Furthermore, for the associated numerical schemes, second-order accuracy is achieved via a two-step procedure in the latter method, involving the solution of two linear systems per time step, as opposed to one single step for IEQ. A check of the order of accuracy, in the case of a scalar nonlinear ODE, is offered in Appendix A.

IEQ for the cases of nonlinear hyperbolic wave equations were proposed in [31] for the sine-Gordon equation, and in [32] for the geometrically exact string, and the results therein are extended here. Other examples of the application of IEQ, of interest in musical acoustics, are given in [33].

3. Semi-discrete formulation

The quadratised equations (16) are now discretised in space, using a mixed formulation including a finite difference discretisation of the transverse waves, and a spectral discretisation of the longitudinal waves. The reason for this design choice resides in the difficulty of resolving a system that comprises two different wave speeds (here, transverse and longitudinal), and whose expressions are obtained after linearisation of (1). The two speeds are, respectively, $c_u = \sqrt{T_0/\rho A}$ (valid at low frequencies), and $c_v = \sqrt{E/\rho}$, where typically $c_v \gg c_u$ for musical strings. Since the grid spacing in a finite difference scheme is directly related to the wave speed via a stability condition, one should consider that adapting the grid spacing to match the velocity in either direction of motion will result in severe frequency warping effects in the other direction, at reference sample rates. One possible solution, proposed e.g. in [8] (Chapter 8) and [34], is to make use of two separate grids, one for the longitudinal and one for the transverse waves, and to perform interpolation in order to couple them. Another choice, explored here, is to make use of a mixed approach: the transverse waves may still be resolved via finite difference schemes; the longitudinal waves may be instead approximated by a suitable modal or spectral discretisation [35, 36].

3.1. Spatial Finite Difference Operators

For the transverse direction, the length L is divided into N subintervals, yielding $N+1$ grid points including the end points. The subintervals are of length $h = L/N$, the grid spacing. Boundary conditions are of fixed type, as per (10), therefore the two end points need not be computed and stored. The physical displacement $u(t, x = mh)$ is approximated by $(\mathbf{u}(t))_m$, $1 \leq m \leq N-1$. The spatial difference operator, for fixed conditions, can be expressed as a $N \times N-1$ matrix of the following form

$$\mathbf{D}^{-}\mathbf{u} = \frac{1}{h}\left([\mathbf{u}^{\intercal}, 0]^{\intercal} - [0, \mathbf{u}^{\intercal}]^{\intercal}\right). \tag{18}$$

The forward and backward spatial difference matrices are related by a transpose operation, i.e.

$$\mathbf{D}^{+} = -\left(\mathbf{D}^{-}\right)^{\intercal}. \tag{19}$$

Furthermore, one has

$$\mathbf{D}^2 = \mathbf{D}^{+}\mathbf{D}^{-}, \qquad \mathbf{D}^4 = \mathbf{D}^2\mathbf{D}^2. \tag{20}$$

i.e. the non-commutative composition of the backward and forward differentiation yields the second spatial difference, and the composition of the second spatial difference with itself gives the fourth spatial difference. Both these matrices are of size $N-1 \times N-1$. Using Taylor-expansion arguments, one has

$$\left(\mathbf{D}^{(+,-)}\mathbf{u}\right)_m = \frac{du(x)}{dx}\Big|_{x=mh} + O(h), \tag{21}$$

$$\left(\mathbf{D}^{2}\mathbf{u}\right)_m = \frac{d^2u(x)}{dx^2}\Big|_{x=mh} + O(h^2), \tag{22}$$

$$\left(\mathbf{D}^{4}\mathbf{u}\right)_m = \frac{d^4u(x)}{dx^4}\Big|_{x=mh} + O(h^2). \tag{23}$$

3.2. Spectral Discretisation of the Longitudinal Waves

For the longitudinal component, one may approximate the continuous function $v(t, x)$ by a grid function $\mathbf{v}(t) : \mathbb{R}_0^+ \to \mathbb{R}^{N-1}$. Then, a spectral operator is applied. This is

$$\mathbf{v}(t) = \mathbf{Z}\mathbf{s}(t). \tag{24}$$

Explicitly, this is given as

$$v_m(t) = \sqrt{\frac{2h}{L}} \sum_{\nu=1}^{N_s} \sin\left(\frac{m\nu h\pi}{L}\right) s_\nu(t) \ , \quad 1 \leq m \leq N-1, \tag{25}$$

Thus, $Z_{m,\nu} = \sqrt{2h/L}\sin(m\nu h\pi/L)$, and the matrix is of size $(N-1)\times N_s$. Here, the upper bound in the sum, N_s, represents the number of eigenfunctions in the longitudinal direction, to be specified later. Note that such basis functions are consistent with the fixed conditions at the string's ends, as per (10). The square root factor multiplying the basis functions is here only a useful normalisation. Here, $\mathbf{Z}$ satisfies the following identities

$$\mathbf{Z}^\intercal \mathbf{Z} = \mathbf{I}, \quad \mathbf{Z}^\intercal \, \mathbf{D}^2 \, \mathbf{Z} = -\mathbf{\Lambda}, \tag{26}$$

where $\mathbf{\Lambda}$ is an $N_s \times N_s$ diagonal matrix with $[\mathbf{\Lambda}]_{\nu,\nu} = \frac{\nu^2\pi^2}{L^2} + O(h^2)$. The first property is a statement of the orthogonality of sine functions; the second property is a consequence of the spectral decomposition of the $\mathbf{D}^2$ operator. These properties can be used to represent the scheme for the longitudinal wave equation in a modal form, as shown below.

3.3. Auxiliary State Variable

The continuous function $\psi(\partial_x u, \partial_x v)$ in (16) will be approximated here as an extra, independent state variable, defined on an interleaved spatial grid, i.e. $\boldsymbol{\psi}(t) : \mathbb{R}_0^+ \to \mathbb{R}^N$. Explicit realisations for (17) must also be supplied. These are given via the vectors $\mathbf{g}_u$, $\mathbf{g}_v$:

$$\mathbf{g}_u = \frac{\sqrt{EA - T_0}\ \mathbf{D}^- \mathbf{u}}{\sqrt{(1 + \mathbf{D}^- \mathbf{v})^2 + (\mathbf{D}^- \mathbf{u})^2}}, \quad \mathbf{g}_v = \frac{\sqrt{EA - T_0}\ (1 + \mathbf{D}^- \mathbf{v})}{\sqrt{(1 + \mathbf{D}^- \mathbf{v})^2 + (\mathbf{D}^- \mathbf{u})^2}}, \tag{27}$$

where the division of vectors, and exponentiation, are intended elementwise. Both these vectors are of length N. From these, the square $N \times N$ matrices $\mathbf{G}_u$ and $\mathbf{G}_v$ are given as

$$\mathbf{G}_u = \mathrm{diag}(\mathbf{g}_u), \quad \mathbf{G}_v = \mathrm{diag}(\mathbf{g}_v). \tag{28}$$

3.4. Semi-discrete Equations of Motion

Using the proposed notation, a semi-discrete realisation of (16) is given as

$$\left(\rho A\frac{d^2}{dt^2} - T_0\mathbf{D}^2 + EI\mathbf{D}^4\right)\mathbf{u}(t) = \mathbf{D}^+\mathbf{G}_u\boldsymbol{\psi}(t), \tag{29a}$$

$$\left(\rho A\frac{d^2}{dt^2} - T_0\mathbf{D}^2\right)\mathbf{Z}\mathbf{s}(t) = \mathbf{D}^+\mathbf{G}_v\boldsymbol{\psi}(t), \tag{29b}$$

$$\frac{d\boldsymbol{\psi}(t)}{dt} = \mathbf{G}_u\left(\frac{d}{dt}\mathbf{D}^-\mathbf{u}(t)\right) + \mathbf{G}_v\left(\frac{d}{dt}\mathbf{D}^-\mathbf{Z}\mathbf{s}(t)\right). \tag{29c}$$

Explicit expressions for $\mathbf{G}_u$, $\mathbf{G}_v$ are given in (28). The longitudinal displacement is expressed as a superposition of modes, as per (24), and diagonalisation of (29b) can be obtained by multiplying on the left by $\mathbf{Z}^\intercal$, to give

$$\left(\rho A\frac{d^2}{dt^2} + T_0\boldsymbol{\Lambda}\right)\mathbf{s}(t) = \mathbf{Z}^\intercal\,\mathbf{D}^+\mathbf{G}_v\boldsymbol{\psi}(t). \tag{30}$$

3.5. Semi-discrete Energy Identities

A discrete version of (4) (inner product and associated norm) for two vectors $\mathbf{f}, \mathbf{g} : \mathbb{R}_0^+ \to \mathbb{R}^{N-1}$ can be given as

$$\langle \mathbf{f}, \mathbf{g}\rangle = h\,\mathbf{f}^\intercal\,\mathbf{g}, \qquad \|\mathbf{f}\| = \sqrt{\langle \mathbf{f}, \mathbf{f}\rangle}. \tag{31}$$

Thus, taking an inner product of (29a) with $\frac{d\mathbf{u}}{dt}$, of (29b) with $\frac{d\mathbf{v}}{dt}$, and summing, yields a semi-discrete energy balance of the kind

$$\frac{d\mathfrak{h}(t)}{dt} = 0 \quad \text{where} \quad \mathfrak{h}(t) = \mathfrak{E}_k(t) + \mathfrak{E}_{pl}(t) + \mathfrak{E}_{pnl}(t). \tag{32}$$

The semi-discrete kinetic, linear and nonlinear potential energies are

$$\mathfrak{E}_k = \frac{\rho A}{2}\left(\left\|\frac{d\mathbf{u}}{dt}\right\|^2 + \left\|\frac{d\mathbf{v}}{dt}\right\|^2\right), \tag{33a}$$

$$\mathfrak{E}_{pl} = \frac{T_0}{2}\left(\left\|\mathbf{D}^-\mathbf{u}\right\|^2 + \left\|\mathbf{D}^-\mathbf{v}\right\|^2\right) + \frac{EI}{2}\left\|\mathbf{D}^2\mathbf{u}\right\|^2, \tag{33b}$$

$$\mathfrak{E}_{pnl} = \frac{\|\boldsymbol{\psi}\|^2}{2}. \tag{33c}$$

which is a non-negative, semi-discrete counterpart of (14). In order to obtain this expression for the energy, the transposition and symmetry properties (19), (20) of the difference matrices were used, along with the rate of change of the auxiliary state variable $\boldsymbol{\psi}$, as per (29c).

4. Time discretisation

A numerical scheme arises after an appropriate time discretisation of (29). Thus, the grid functions $\mathbf{u}(t), \mathbf{v}(t)$ are approximated at the time nk by the time series $\mathbf{u}^n, \mathbf{v}^n$, where $n \in \mathbb{N}_0$, and where k is the time step (the multiplicative inverse of the sample rate). Similarly, the auxiliary state variable $\boldsymbol{\psi}(t)$ is approximated by an interleaved time series $\boldsymbol{\psi}^{n-1/2}$.

4.1. Time Difference Operators

The basic operators in discrete time are the identity and shift operators, defined as

$$1\mathbf{u}^n = \mathbf{u}^n, \quad e_{t+}\mathbf{u}^n = \mathbf{u}^{n+1}, \quad e_{t-}\mathbf{u}^n = \mathbf{u}^{n-1}. \tag{34}$$

From these, one may define the time difference operators, all approximating the first time derivative, as

$$\delta_{t+}\mathbf{u}^n = \frac{(e_{t+} - 1)\mathbf{u}^n}{k} = \frac{d\mathbf{u}(t)}{dt}\Big|_{t=kn} + O(k), \tag{35a}$$

$$\delta_{t-}\mathbf{u}^n = \frac{(1 - e_{t-})\mathbf{u}^n}{k} = \frac{d\mathbf{u}(t)}{dt}\Big|_{t=kn} + O(k), \tag{35b}$$

$$\delta_{t\cdot}\mathbf{u}^n = \frac{(e_{t+} - e_{t-})\mathbf{u}^n}{2k} = \frac{d\mathbf{u}(t)}{dt}\Big|_{t=kn} + O(k^2). \tag{35c}$$

An approximation to the second time derivative is constructed from the above as

$$\delta_{tt}u^n = (\delta_{t+}\delta_{t-})\mathbf{u}^n = \frac{d^2\mathbf{u}(t)}{dt^2}\Big|_{t=kn} + O(k^2). \tag{36}$$

Averaging operators are also used throughout the text, and are

$$\mu_{t+}\mathbf{u}^n = \frac{(e_{t+} + 1)\mathbf{u}^n}{2} = \mathbf{u}(kn) + O(k), \tag{37a}$$

$$\mu_{t-}\mathbf{u}^n = \frac{(1 + e_{t-})\mathbf{u}^n}{2} = \mathbf{u}(kn) + O(k), \tag{37b}$$

$$\mu_{t\cdot}\mathbf{u}^n = \frac{(e_{t+} + e_{t-})\mathbf{u}^n}{2} = \mathbf{u}(kn) + O(k^2). \tag{37c}$$

For the interleaved function $\boldsymbol{\psi}^{n-1/2}$, the same definitions apply formally, but the order of the approximation changes. Thus

$$1\boldsymbol{\psi}^{n-1/2} = \boldsymbol{\psi}^{n-1/2}, \quad e_{t+}\boldsymbol{\psi}^{n-1/2} = \boldsymbol{\psi}^{n+1/2}. \tag{38}$$

The time difference is

$$\delta_{t+}\boldsymbol{\psi}^{n-1/2} = \frac{(e_{t+}-1)\boldsymbol{\psi}^{n-1/2}}{k} = \frac{d\boldsymbol{\psi}(t)}{dt}\Big|_{t=kn} + O(k^2), \tag{39}$$

and the averaging operator gives

$$\mu_{t+}\boldsymbol{\psi}^{n-1/2} = \frac{(e_{t+}+1)\boldsymbol{\psi}^{n-1/2}}{2} = \boldsymbol{\psi}(kn) + O(k^2). \tag{40}$$

and note that the following identity, used throughout the text, holds

$$\mu_{t+}\boldsymbol{\psi}^{n-1/2} = \frac{k}{2}\delta_{t+}\boldsymbol{\psi}^{n-1/2} + \boldsymbol{\psi}^{n-1/2} \tag{41}$$

Three useful identities are given here. Considering the inner product and norm given in (31), one has

$$\langle \delta_{t\cdot}\mathbf{u}, \delta_{tt}\mathbf{u}\rangle = \delta_{t+}\frac{\|\delta_{t-}\mathbf{u}\|^2}{2}, \tag{42a}$$

$$\langle \mathbf{u}, \delta_{t\cdot}\mathbf{u}\rangle = \delta_{t+}\frac{\langle \mathbf{u}, e_{t-}\mathbf{u}\rangle}{2}, \tag{42b}$$

$$\langle \delta_{t+}\boldsymbol{\psi}, \mu_{t+}\boldsymbol{\psi}\rangle = \delta_{t+}\frac{\|\boldsymbol{\psi}\|^2}{2}. \tag{42c}$$

4.2. Fully-discrete Equations of Motion

Given the above definitions, a fully-discrete system of equations can now be given. These are

$$\left(\rho A\delta_{tt} - T_0\mathbf{D}^2 + (1+\eta(\mu_{t\cdot}-1))EI\mathbf{D}^4\right)\mathbf{u}^n = \mathbf{D}^+\mathbf{G}_u^n\ \mu_{t+}\boldsymbol{\psi}^{n-1/2}, \tag{43a}$$

$$\left(\rho A\delta_{tt} + T_0\boldsymbol{\Lambda}\right)\mathbf{s}^n = \mathbf{Z}^\intercal\mathbf{D}^+\mathbf{G}_v^n\ \mu_{t+}\boldsymbol{\psi}^{n-1/2}, \tag{43b}$$

$$\delta_{t+}\boldsymbol{\psi}^{n-1/2} = \mathbf{G}_u^n\left(\delta_{t\cdot}\mathbf{D}^-\mathbf{u}^n\right) + \mathbf{G}_v^n\left(\delta_{t\cdot}\mathbf{D}^-\mathbf{Z}\mathbf{s}^n\right). \tag{43c}$$

which discretises (29). Note that $\mathbf{G}_u^n$, $\mathbf{G}_v^n$ are given by (28), after substituting $\mathbf{u}(t) \to \mathbf{u}^n$, $\mathbf{v}(t) \to \mathbf{v}^n$. In (43a) , $\eta \in \{0, 1\}$: when $\eta = 0$, the fourth-order spatial operator is discretised explicitly. As will be seen shortly, this has consequences on the stability, efficiency and convergence properties of the scheme, as well as on its wideband behaviour in the frequency domain. All these aspects will be investigated thoroughly in the following sections.

Furthermore, it is remarked that this scheme is a three-step scheme, in that not only does one need to solve for the displacement $\mathbf{u}$, and modal

coordinates $\mathbf{s}$, but also for $\boldsymbol{\psi}$, which is treated here as an auxiliary state variable. Thus, the numerical system is here completed by a set of initial conditions on $\mathbf{u}, \mathbf{v}$ discretising (3), (from which one may get $\mathbf{s} = \mathbf{Z}^\intercal \mathbf{v}$), as well as a suitable initial condition for $\boldsymbol{\psi}$, which can be given as

$$\boldsymbol{\psi}^{1/2} = \sqrt{EA - T_0} \left(\sqrt{\left(1 + \mathbf{D}^- \mathbf{Z} \mu_{t+} \mathbf{s}^0\right)^2 + \left(\mathbf{D}^- \mu_{t+} \mathbf{u}^0\right)^2} - 1 \right). \tag{44}$$

Note that the averaging operators are here used so to yield a second-order accurate discretisation of the continuous function ψ, at the initial interleaved time step $t_{1/2} = k/2$.

The time discretisation was chosen here such that (43) conserves a numerical energy. This is easily shown after taking an inner product (as per (31)) of (43a) with $\delta_{t\cdot}\mathbf{u}$, of (43b) with $\delta_{t\cdot}\mathbf{v}$, summing, and making use of (43c) plus the identities given in (42), as well as definition (25) and identities (26). The result is

$$\delta_{t+} \mathfrak{h}^{n-1/2} = 0, \quad \text{where} \quad \mathfrak{h} = \mathfrak{E}_k + \mathfrak{E}_{pl} + \mathfrak{E}_{pnl}. \tag{45}$$

The kinetic, linear and nonlinear potential energies are given as

$$\mathfrak{E}_k^{n-1/2} = \frac{\rho A}{2} \left(\|\delta_{t-} \mathbf{u}^n\|^2 + \|\delta_{t-} \mathbf{v}^n\|^2 \right) + \frac{\eta E I k^2}{4} \|\mathbf{D}^2 \delta_{t-} \mathbf{u}^n\|^2, \tag{46a}$$

$$\mathfrak{E}_{pl}^{n-1/2} = \frac{T_0}{2} \left(\left\langle \mathbf{D}^- \mathbf{u}^n, \mathbf{D}^- e_{t-} \mathbf{u}^n \right\rangle + \left\langle \mathbf{D}^- \mathbf{v}^n, \mathbf{D}^- e_{t-} \mathbf{v}^n \right\rangle \right) + \frac{EI}{2} \left\langle \mathbf{D}^2 \mathbf{u}^n, \mathbf{D}^2 e_{t-} \mathbf{u}^n \right\rangle, \tag{46b}$$

$$\mathfrak{E}_{pnl}^{n-1/2} = \frac{\left\| \boldsymbol{\psi}^{n-1/2} \right\|^2}{2}. \tag{46c}$$

This expression approximates the total energy of the system. As opposed to the continuous and the semi-discrete cases (14) and (33), the fully-discrete expression for the energy may be negative in some cases. Non-negativity is achieved here only when the grid spacing h and the time step k satisfy a suitable condition, arising as a consequence of the discretisation of the linear part (since the nonlinear energy, from (46c), is non-negative by definition). When k is selected as input parameter, lower bounds on h are given as (see

e.g. [8, 37])

$$h \geq \begin{cases} \sqrt{\dfrac{T_0 k^2 + \sqrt{(T_0 k^2)^2 + 16\rho A E I k^2}}{2\rho A}} \triangleq h_0, & \text{if } \eta = 0, \quad (47a) \\ \sqrt{\dfrac{T_0}{\rho A}}\, k \triangleq h_{CFL}, & \text{if } \eta = 1. \quad (47b) \end{cases}$$

It is remarked that the stability condition for $\eta = 0$ is not a pure CFL condition, since the time step is not directly proportional to the grid spacing. This is a consequence of the explicit discretisation of the fourth spatial derivative, i.e. $\partial_x^4 u(t,x) \rightarrow \mathbf{D}^4\,\mathbf{u}^n$. This discretisation has the benefit of reducing the number of grid points, at the stability limit, when the time step is chosen as input parameter.

When conditions (47) are enforced, the energy is non-negative, and hence the grid functions remain bounded over time, with bounds holding here as discrete versions of (12):

$$0 \leq \|\delta_{t-}\mathbf{u}^n\| \leq \sqrt{2\mathfrak{h}^{1/2}/\rho A}, \quad 0 \leq \left\|\mu_{t-}\mathbf{D}^-\mathbf{u}^n\right\| \leq \sqrt{2\mathfrak{h}^{1/2}/T_0}, \tag{48}$$

with similar bounds holding for the longitudinal grid function $\mathbf{v}$. It is remarked that the auxiliary state variable $\boldsymbol{\psi}$ remain itself bounded, as

$$0 \leq \left\|\boldsymbol{\psi}^{n-1/2}\right\| \leq \sqrt{2\mathfrak{h}^{1/2}}. \tag{49}$$

4.3. Number of Numerical Longitudinal Eigenfunctions

A bound on the number of longitudinal eigenfunctions, determining the size of $\mathbf{Z}$ in (24), can be derived by imposing non-negativity of the longitudinal linear discrete energy, i.e. $N_s \leq (2L/\pi k)\sqrt{\rho A/T_0}$ [8] (Chapter 6). It will be convenient, however, to use a much lower number of modes, such that

$$N_s \leq \frac{2L}{\pi k}\sqrt{\frac{\rho}{E}}. \tag{50}$$

This is the natural bound on the number of modes associated with the CFL condition on the longitudinal wave speed $c_v = \sqrt{E/\rho}$. This choice has the benefit of efficiency, since the system is much smaller in size (typically $c_v \gg c_v$).

4.4. Solvability, Local Truncation Error and Convergence

Solving system (43) is accomplished by first using identity (41) in both (43a) and (43b), and then using (43c) to express the $\delta_{t+}\boldsymbol{\psi}$ in terms of $\mathbf{u}$, $\mathbf{s}$. The resulting system is written as

$$\mathbf{T}\begin{bmatrix}\mathbf{u}^{n+1}\\ \mathbf{s}^{n+1}\end{bmatrix} = \begin{bmatrix}\mathbf{b}_u^n\\ \mathbf{b}_s^n\end{bmatrix}, \tag{51}$$

where $\mathbf{T} = \mathbf{T}_0 - \tilde{\mathbf{T}}^n$, and

$$\mathbf{T}_0 = \begin{bmatrix}\frac{\rho A}{k^2}\mathbf{I} + \frac{\eta EI}{2}\mathbf{D}^4 & \mathbf{0}\\ \mathbf{0} & \frac{\rho A}{k^2}\mathbf{I}\end{bmatrix} \tag{52a}$$

$$\tilde{\mathbf{T}}^n = \frac{1}{4}\begin{bmatrix}\mathbf{D}^+\mathbf{G}_u^n\mathbf{G}_u^n\mathbf{D}^- & \mathbf{D}^+\mathbf{G}_u^n\mathbf{G}_v^n\mathbf{D}^-\mathbf{Z}\\ \mathbf{Z}^\intercal\mathbf{D}^+\mathbf{G}_u^n\mathbf{G}_v^n\mathbf{D}^- & \mathbf{Z}^\intercal\mathbf{D}^+\mathbf{G}_v^n\mathbf{G}_v^n\mathbf{D}^-\mathbf{Z}\end{bmatrix}. \tag{52b}$$

Here, $\mathbf{b}_u^n$, $\mathbf{b}_s^n$ are vectors of known coefficients from previous time steps, of length $N-1$ and N_s respectively. The update matrix is the sum of a time-independent matrix $\mathbf{T}_0$, accounting for the linear part of the system, minus a time-dependent matrix $\tilde{\mathbf{T}}^n$, accounting for the nonlinearities (and which must be recomputed at each time step). Note that $\mathbf{T}$ is a non-singular, symmetric matrix, and therefore $\mathbf{u}^{n+1}$, $\mathbf{s}^{n+1}$ are uniquely determined. These values can then be used to compute $\mathbf{v}^{n+1}$ via (24), and $\boldsymbol{\psi}^{n+1/2}$ via (43c). The top left square block in $\mathbf{T}$ is sparse, and it contains the most elements in the matrix. The bottom right square block is the smallest, and is full. The off-diagonal rectangular blocks are also full. It is convenient to approach the solution of the linear system by decomposing the matrix $\mathbf{T}$ using the Schur complement, as detailed below in Section 5.

The local truncation error τ_m^n of scheme (43) at time $t_n = nk$ and at the grid point $x_m = mh$ is obtained when the scheme is applied to the true solutions $u(t,x), v(t,x)$ of (16), and Taylor-expanding, see e.g. [38]. Using the Taylor expansions given above for the spatial and temporal operators, it can be shown that

$$\tau_m^n = O(h^2) + O(k^2), \tag{53}$$

When k and h are chosen along the path dictated by the stability condition (47), one has $k = O(h^2)$ when $\eta = 0$, making the scheme formally first-order convergent in the time step k. For $\eta = 1$, the scheme is second-order accurate in both k and h. Space-time convergence curves for both $\eta = 0, 1$, in the linear case, are given in Appendix B. One may go further and prove convergence of

the nonlinear system as a consequence of stability and consistency, showing that the scheme converges to the true solution as h, k tend to zero, and that the global error preserves the same order accuracy when h, k are decreased along the path given by the stability condition. This is a delicate point: one should be wary that theoretical error estimate blow-ups have been predicted, even for linear wave equations, see e.g. [39, 40]. In [39], it is shown that a post-processing of the error time series leads indeed to an estimate that does not blow up, in accordance with empirical observations. Here, a formal proof for the proposed scheme, while necessary, is out-of-scope. A proof of order-accuracy in the case of a hyperbolic wave equation as per the sine-Gordon model, using IEQ, is given in [31]. Other formal proofs of applications of IEQ are included in e.g. [21].

5. Computational Testing

A mentioned above, a suitable matrix decomposition may be employed to speed up the solution of the linear system (51). First, write

$$\mathbf{T} = \begin{bmatrix} \mathbf{T}_{11} & \mathbf{T}_{12} \\ \mathbf{T}_{12}^{\intercal} & \mathbf{T}_{22} \end{bmatrix}. \tag{54}$$

Here, $\mathbf{T}_{11}$ is an $N-1 \times N-1$ sparse block, $\mathbf{T}_{12}$ is an $N-1 \times N_s$ full block, and $\mathbf{T}_{22}$ is a $N_s \times N_s$ full block. For typical strings, when one chooses the grid spacing according to (47), one has $N_s \ll N$ and it results therefore natural to decompose the matrix so to take advantage of the sparsity of the largest block $\mathbf{T}_{11}$. Block LDU factorisation [41] is one such matrix decomposition algorithm. This is

$$\mathbf{T} = \begin{bmatrix} \mathbf{I} & \mathbf{0} \\ \mathbf{T}_{12}^{\intercal}\mathbf{T}_{11}^{-1} & \mathbf{I} \end{bmatrix} \begin{bmatrix} \mathbf{T}_{11} & \mathbf{0} \\ \mathbf{0} & \boldsymbol{\kappa} \end{bmatrix} \begin{bmatrix} \mathbf{I} & \mathbf{T}_{11}^{-1}\mathbf{T}_{12} \\ \mathbf{0} & \mathbf{I} \end{bmatrix} \tag{55}$$

where

$$\boldsymbol{\kappa} = \mathbf{T}_{22} - \mathbf{T}_{12}^{\intercal}\mathbf{T}_{11}^{-1}\mathbf{T}_{12} \tag{56}$$

is called the Schur complement, and is here a $N_s \times N_s$ full matrix. Remembering the definitions of $\mathbf{b}_u^n$, $\mathbf{b}_s^n$ from (51), an efficient algorithm may be extracted from the decomposition above as follows. First, define

$$\mathbf{y} = \mathbf{T}_{11}^{-1}\mathbf{b}_u^n, \tag{57a}$$

$$\mathbf{z} = \mathbf{b}_s^n - \mathbf{T}_{12}^{\intercal}\mathbf{y}. \tag{57b}$$

Then, the solution to (51) is obtained as

$$\mathbf{s}^{n+1} = \boldsymbol{\kappa}^{-1}\mathbf{z}, \tag{58a}$$

$$\mathbf{u}^{n+1} = \mathbf{y} - \mathbf{T}_{11}^{-1}\mathbf{T}_{12}\,\mathbf{s}^{n+1}. \tag{58b}$$

This algorithm requires the solution of three linear systems: two are sparse (one in (57a), one in (58b)), and one is full (in (58a)), though of very small size. A sparse matrix inversion is also required to compute $\boldsymbol{\kappa}$ in (56).

The proposed algorithm (denoted `LU_NIT`) is now compared against the two schemes presented in [32]. These are: 1. a non-iterative scheme (denoted `ICA_NIT`) obtained from the same quadratisation proposed here, but where both the transverse and the longitudinal waves are simulated using finite differences in both space and time; 2. an iterative finite difference scheme (denoted `ICA_IT`) obtained using a fully-implicit discretisation of the gradient, in a way that is analogous to that employed in numerous works, see e.g. [42, 29, 17, 43]. Since in [32] stiffness is not considered, in this test I is set to zero, and the choice of η in (43a) has no influence. Note as well that both `LU_NIT` and `ICA_NIT` are in the form of "quadratised" schemes, the only differences being in the discretisation of the longitudinal component, as well as in the linear system solver employed. For the iterative scheme `ICA_IT`, the number of iterations is set using a tolerance threshold $\tau = 10^{-13}$ on the computed iteration, and the maximum number of iterations is capped at 100. The test is run on a 2016 Macbook Pro equipped with a 2.9GHz Intel Core i7 processor. The algorithms are implemented and run in Matlab2020. Unless otherwise specified, all the linear systems and the matrix inversions are implemented using Matlab's backslash (\). Source code is available on the companion webpage[1]. A summary of the string's parameters employed here is given in Table 1.

Two tests are run, summarised in Tables 2 and 3. The string is initialised with a centered raised cosine, with an initial maximum amplitude of 2 mm, (as in Figure 1 below). The amplitude is chosen so that nonlinear effects are clearly audible. In the first test, the sample rate is chosen as input parameter, and the grid spacing is chosen as $h = 1.05h_{CFL}$, where h_{CFL} is given in (47b) (slightly away from the limit of stability of the transverse waves). In the second test, the grid spacing is chosen at the limit of stability of the longitudinal waves, i.e. $h = \sqrt{E/\rho}\,k$, that is, the same as in [32] (note

[1] https://mdphys.org/JSV_2022.html

	units	value
ρ	$\mathrm{kg/m^3}$	8000
E	Pa	$2 \cdot 10^{11}$
T_0	N	40
L	m	1
r	mm	0.29

Table 1: String parameters, obtained from typical values for musical strings.

that this is a much larger spacing than in the previous test). Compared to the `ICA_IT` scheme, both non-iterative schemes give consistent speedups, particularly when the grid spacing is smaller. In this respect, note that the computational speedup of the LU decomposition is less pronounced as the ratio N/N_s becomes smaller (i.e., the grid spacing becomes larger), since sparsity of the matrix $\mathbf{T}$ is reduced. Furthermore, in this test `LU_NIT` is also faster than the previously availble `ICA_NIT`, though here the compute time ratio is almost constant ascross all tests.

OF	N	N_s	`LU_NIT` (s)	`ICA_NIT` (s)	`ICA_IT` (s)	$\frac{\texttt{ICA\_IT}}{\texttt{LU\_NIT}}$	$\frac{\texttt{ICA\_IT}}{\texttt{ICA\_NIT}}$	$\frac{\texttt{ICA\_NIT}}{\texttt{LU\_NIT}}$
1	332	7	0.35	0.48	1.29	3.7	2.7	1.4
2	664	13	1.67	2.37	7.58	4.5	3.2	1.4
4	1329	25	14.6	22.3	83.2	5.7	3.7	1.5

Table 2: Compute times for 0.01 seconds of output. The string parameters are as in Table 1 and initial conditions considered here are the same as Figure 1. The oversampling factors (OF) are given for a base sample rate $f_s = 48 \cdot 10^3$ Hz. The grid spacing is chosen as $h = 1.05\sqrt{T_0/\rho A}\,k$. The iterative scheme is run with a tolerance threshold 10^{-13}, and 100 maximum iterations per step. The compute times reported are an average over 5 consecutive tests.

5.1. Experiments

The performance of scheme (43) is now assessed in a numerical experiment. In Figure 1, one can see the snapshots of the time evolution of the simulation, at successive times. The string is initialised in the transverse direction with a raised cosine distribution centered around the midpoint of the problem domain. In this example, the moment of inertia I is set to

OF	N	N_s	LU_NIT (s)	ICA_NIT (s)	ICA_IT (s)	$\frac{\texttt{ICA\_IT}}{\texttt{LU\_NIT}}$	$\frac{\texttt{ICA\_IT}}{\texttt{ICA\_NIT}}$	$\frac{\texttt{ICA\_NIT}}{\texttt{LU\_NIT}}$
1	9	7	0.04	0.06	0.11	2.7	1.8	1.5
2	19	13	0.09	0.12	0.23	2.6	1.9	1.3
4	38	25	0.23	0.30	0.52	2.3	1.7	1.3

Table 3: Same as Table 2, but here the grid spacing is chosen as $h = \sqrt{E/\rho}\,k$.

zero, so to compare LU_NIT against both the linear one-dimensional wave equation, and to the iterative finite-difference scheme ICA_IT presented in [32]. The key features of nonlinear wave propagation relative to linear are increased wave speed, as well as a progressive flattening of the peaks with time. Notice that both schemes (43) and the iterative scheme from [32] yield consistent solutions. The same observations can be drawn from results shown in Figure 2. The top panel is a representation of the same solutions for the transverse displacement, but plotted against time. The second panel instead shows the longitudinal displacement: the two models yield again consistent results, though differences are noticeable. Energy remains conserved for both schemes, with an error of the order of machine accuracy. However, the iterative scheme can only achieve this through a large number of iterations, highlighting the advantage of the linearly-implicit formulation (51).

Note that, in the simulation, the grid spacing is chosen to be slightly larger than bound (47b) satisfied with equality. This is to avoid possible erratic behaviour near Nyquist. In practice, some spurious noise is generated by the schemes, and propagated through the spectrum by the nonlinear coupling. This is not a blow-up, rather, it is a polluted solution. This effect has been observed for other nonlinear systems, see for example the Kirchhoff-Carrier string in [8] (Chapter 8).

6. Wideband Numerical Dispersion Reduction

Numerical dispersion introduces artefacts in the computed solution. In the linear case, modified-equation techniques can be employed to increase the formal order of accuracy of the numerical schemes, see e.g. [44, 45, 46, 47, 48]. Dispersion is a frequency-dependent effect, and higher frequencies are usually more affected by it. Order-accuracy holds in the low-frequency limit, and it was observed that lower-order accurate schemes may yield better wideband behaviour, see e.g. [49, 50]. For this reason, it may be preferable to reduce

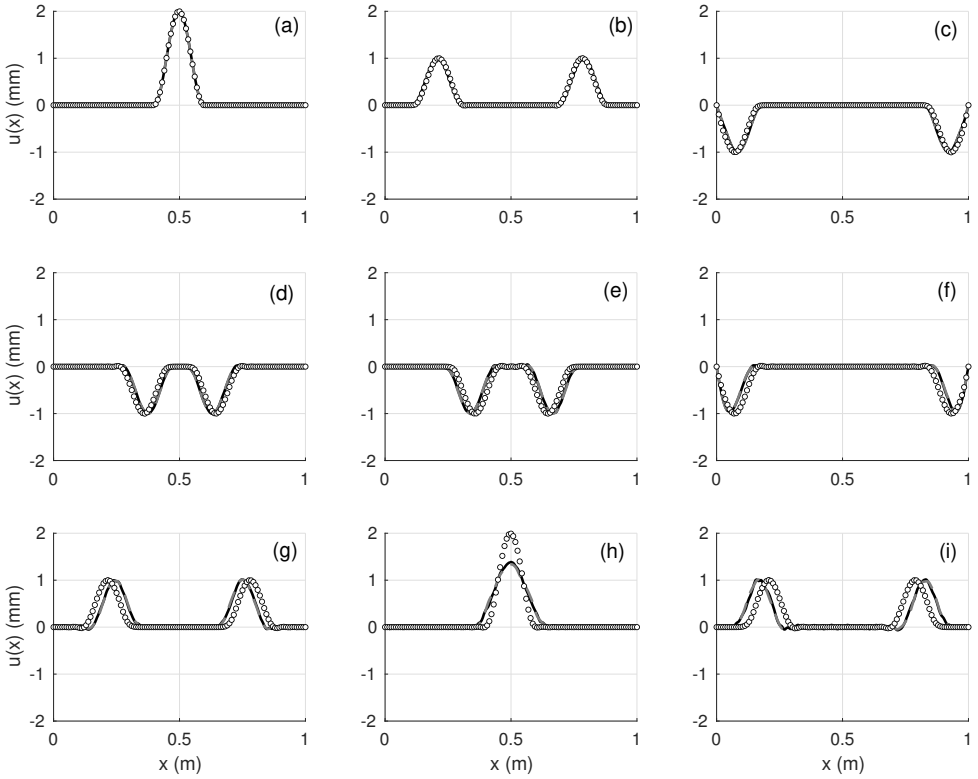

Figure 1: Snapshots of the time evolution of solutions to the nonlinear wave equation, at successive times. For all panels, the circles represent the solution to the linear wave equation, the thick black line is the iterative finite difference scheme `ICA_IT` presented in [32], and the dashed grey line is `LU_NIT` (43). Note that stiffness was not considered in this example, so $I = 0$. The string has the parameters listed in Table 1. The solutions are initialised with a raised cosine distribution with compact support of the form $u(0,x) = \frac{U_0}{2}\left(1+\cos\left(\frac{2\pi(x-L/2)}{2\sigma L}\right)\right)$ for $L/2-\sigma L \leq x \leq L/2+\sigma L$, and $u(0,x) = 0$ elsewhere. Here, $U_0 = 2$ mm and $\sigma = 0.1$. The sample rate used is $f_s = 48$ kHz, and the grid spacing is $h = 1.05h_{CFL}$, where h_{CFL} is as per (47b).

dispersion over the entire range of frequencies [51, 37], rather than increasing the formal order of accuracy. As an example, consider Figure 3. There, the numerical dispersion relations of the linear part of (43a) are compared against the continuous dispersion relation of the linear part of (1a). Remember that, from the discussion in Section 4.4, the error of the scheme with $\eta = 1$ is second-order in both k and h. For $\eta = 0$, the error is second-order in h and first-order in k. (These estimates are true when the stability conditions

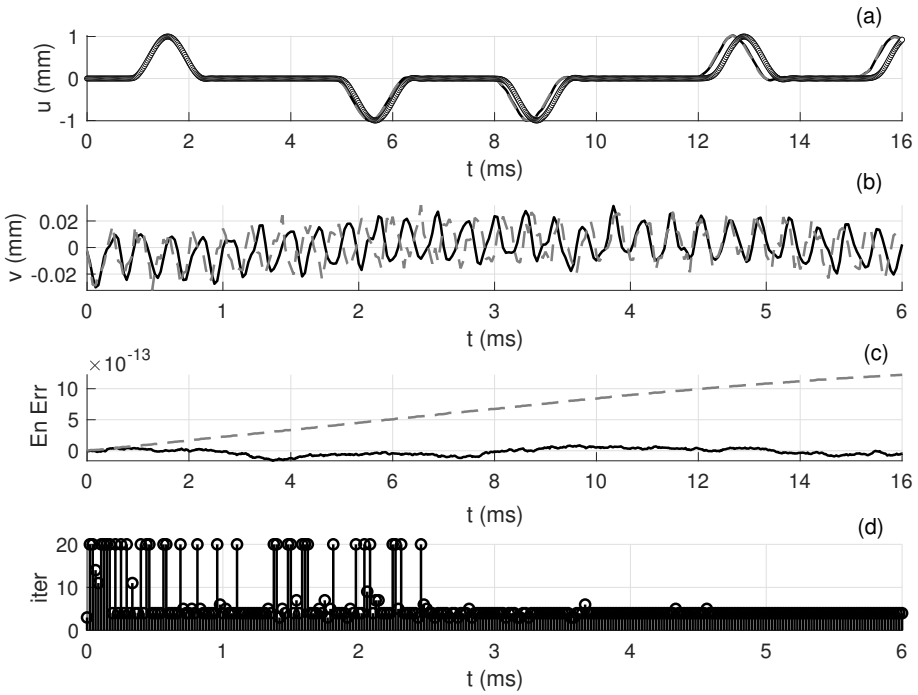

Figure 2: Waveforms and energy error. The circles represent the solution to the linear wave equation, the thick black line is the iterative finite difference scheme `ICA_IT` from [32], and the dashed grey line is the non-iterative scheme `LU_NIT` (43). (a): transverse displacement, output is taken at $x_o = 0.72L$; (b): longitudinal displacement, output is taken at $x_o = 0.72L$; (c): energy error for both schemes, defined as $\epsilon^{n-1/2} = 1 - \mathfrak{h}^{n-1/2}/\mathfrak{h}^{1/2}$; (d): number of iterations for the transverse Newton-Raphson, with a tolerance threshold $\tau = 10^{-13}$, and escape condition iter ≤ 20.

(47) are satisfied near equality, see also Appendix B). While the scheme with $\eta = 1$ is higher-accurate in k, its wideband dispersion properties are somewhat worse, as seen in Figure 3. In other words, when both schemes are run with the same sample rate, and the grid spacings are chosen close to bounds (47), the increased accuracy of scheme with $\eta = 1$ at lower frequencies quickly deteriorates at higher frequencies. For audio, it may be preferable to mantain low numerical dispersion across a wideband portion of the spectrum, rather than higher order-accuracy, since numerical dispersion in the mid-high range results in a detuning of higher partials [8] (Chapter 7). For this reason, in the remainder, the scheme with $\eta = 1$ will be dismissed. The idea is to now employ a parametrised version of (43a), with $\eta = 0$, so to reduce numerical

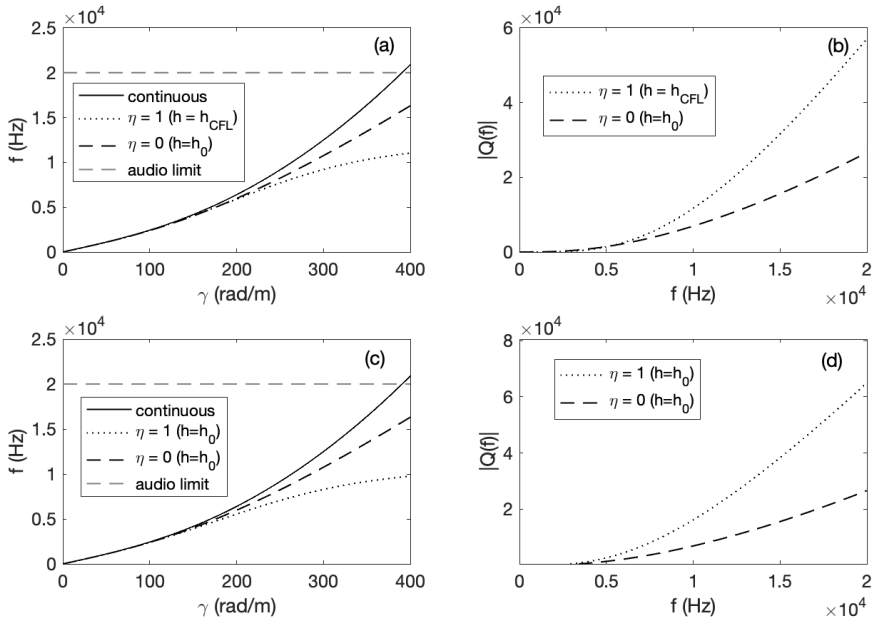

Figure 3: Continuous and numerical dispersion relations. The numerical dispersion relations are obtained from the linear part of (43a) (left-hand side), using $\eta = 0$ and $\eta = 1$, and by transforming the difference operators in the frequency domain, as $\mathbf{D}^2 \to -4/h^2 \sin^2(\gamma h/2)$, $\mathbf{D}^4 \to 16/h^4 \sin^4(\gamma h/2)$, $\delta_{tt} \to -4/k^2 \sin^2(\omega k/2)$, and using $\mu_{t\cdot} = 1 + \frac{k^2}{2}\delta_{tt}$. Here, γ is the wavenumber, and ω is the radian frequency (though the linear frequency $f = \omega/2\pi$ is plotted), and h_0, h_{CFL} are given in (47). Panels (a) and (b) plot the dispersion relation and the absolute value of the error $Q(f)$ (i.e. the difference between the continuous and numerical dispersion relations) for the schemes with $\eta = 0$ and $\eta = 1$, when they are both run at their respective limits of stability given in (47). The sample rate is $f_s = 48 \cdot 10^3$, and the string parameters are given in Table 1. Panels (c) and (d) repeat the same experiments, except that the scheme with $\eta = 1$ is run at the limit of stability of the scheme with $\eta = 0$. Note that, in both cases, $\eta = 0$ yields lower wideband numerical dispersion.

dispersion across a large portion of the frequency axis. To that end, consider the following modification of the linear part of (43a):

$$\left(\rho A \mathbf{R}(\theta_u)\delta_{tt} - T_0\mathbf{D}^2 + EI\mathbf{D}^4\right)\mathbf{u}^n = 0, \tag{59}$$

where the parameterised operator $\mathbf{R}(\theta_u)$ has the form

$$\mathbf{R}(\theta_u) = \mathbf{I} + \frac{(1-\theta_u)h^2}{2}\mathbf{D}^2. \tag{60}$$

One can select θ_u so that the number of grid intervals matches the number of eigenfunctions whose eigenfrequency is found below the Nyquist limit $1/2k$, resulting in wideband dispersion reduction, see e.g. [8] (Chapter 7), and [37]. Let such number of eigenfunctions be N_u. Under simply-supported conditions,

$$N_u = \frac{L}{\pi}\sqrt{\frac{-T_0 + \sqrt{T_0^2 + \frac{4\pi^2}{k^2}\rho E A I}}{2EI}} \tag{61}$$

Then, one selects (see [37])

$$\theta_u = \bar{\theta}_u \triangleq \frac{1}{2} + \frac{T_0 k^2 \bar{h}^2 + 4EIk^2}{2\rho A \bar{h}^4}, \quad \text{with } \bar{h} = \frac{L}{N_u}. \tag{62}$$

The numerical transverse eigenfrequencies ω_m, $1 \leq m \leq N-1$ of the parameterised scheme can be determined through use of the ansatz $\mathbf{u}^n = e^{j\omega nk}\hat{\mathbf{u}}$, for a constant vector $\hat{\mathbf{u}}$, and angular frequency ω, as

$$\{\omega_m\} = \frac{2}{k}\arcsin\left(\frac{k}{2}\text{eig}\left[\mathbf{R}(\theta_u)^{-1}\left(-\frac{T_0}{\rho A}\mathbf{D}^2 + \frac{EI}{\rho A}\mathbf{D}^4\right)\right]^{1/2}\right). \tag{63}$$

Figure 4 shows the numerical dispersion relations and the modal frequencies for various choices of the parameter θ_u. It can be seen that, under the choice (62), the warping effects are minimised across the spectrum, though order-accuracy is not formally decreased (since the correction factor is itself $O(h^2)$), when the stability condition is fulfilled close to the stability limit (though one must be wary of theoretical error-estimates blow-ups, as explained in e.g. [39] for the case of linear wave equations; see also comment in the last paragraph of Section 4.4). The same figure shows the results obtained when one chooses h as per the natural longitudinal grid spacing $h_v = \sqrt{E/\rho}\, k$: frequency warping effects are evident, and one is not able to resolve frequencies above a few hundred Hz, at audio rate. This highlights the benefits of the choice of the nonlinear potential function ϕ in (2), which leaves the linear part of the transverse waves unaffected. Convergence of the eigenfrequencies (63), as well as space-time convergence curves for the parameterised linear scheme (59) are given in Appendix C.

The discrete energy is modified by the introduction of the operator $\mathbf{R}(\theta_u)$. A correction of the order $O(h^2)$ appears in the kinetic term (46a), which now reads

$$\mathfrak{E}_k = \frac{\rho A}{2}\left(\|\delta_{t-}\mathbf{u}\|^2 + \|\delta_{t-}\mathbf{v}\|^2 + \frac{(\theta_u - 1)h^2}{2}\left\|\mathbf{D}^-\delta_{t-}\mathbf{u}\right\|^2\right).$$

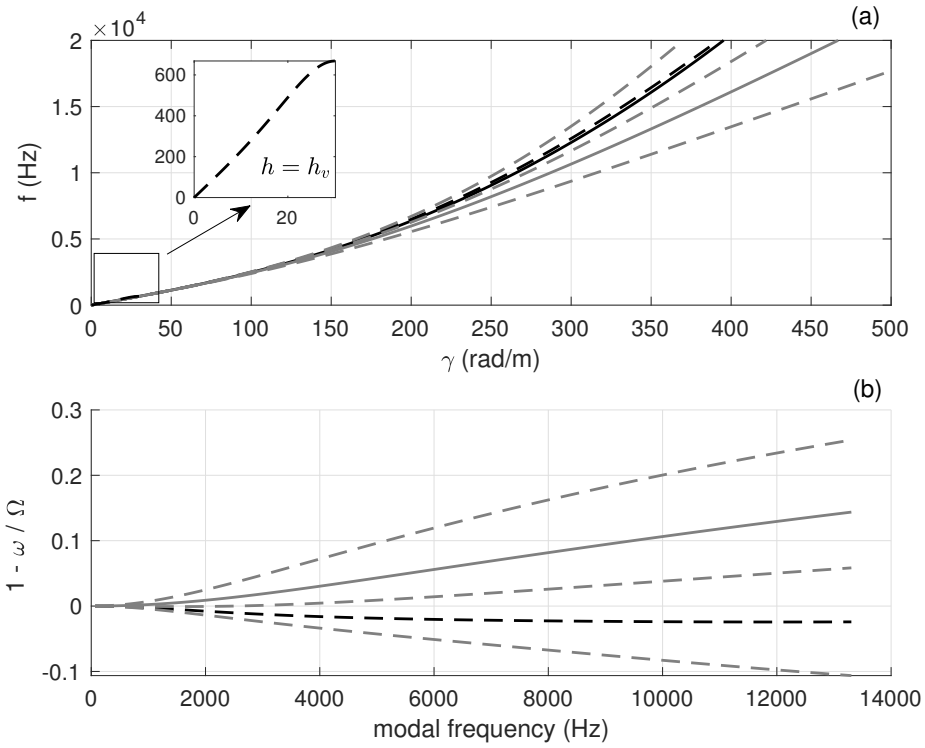

Figure 4: Numerical dispersion relation and error on modal frequencies of the linear transverse displacement. The string parameters are as per Table 1. The sample rate is $f_s = 48$ kHz. (a): Dispersion relations. Black solid line is the continuous dispersion relation; black dashed line is obtained using the stability condition (64) using $\theta_u = \bar{\theta}_u$ given in (62); grey solid line is obtained with $\theta_u = 1$; grey dashed lines are obtained under various other choices for θ_u. The choice of the longitudinal grid spacing $h = h_v = \sqrt{E/\rho}\, k$ is also given in the inset. (b): error on modal frequencies. Black dashed line is obtained using the stability condition (64) using $\theta_u = \bar{\theta}_u$ given in (62); grey solid line is obtained with $\theta_u = 1$; grey dashed lines are obtained under various other choices for θ_u. The numerical frequencies ω are as per (63). The analytic frequencies Ω are given in (B.3).

This imposes a modification of the stability condition (47a), which now is

$$h \geq h_0(\theta_u) \triangleq \sqrt{\frac{T_0 k^2 + \sqrt{(T_0 k^2)^2 + 16(2\theta_u - 1)\rho A E I k^2}}{2\rho A(2\theta_u - 1)}}, \tag{64}$$

where it is assumed that $\theta_u > 1/2$. Though the value for θ_u was selected in the lossless case, losses are small for musical strings, and hence the wideband dispersion properties are mostly unaffected by it.

7. Application: the nonlinear struck, damped string

The stiff string model detailed in Section 2 is here extended to include simple loss and source terms, for illustrative purposes. The equations of motion of such system, an extension of (16), are

$$\left(\rho A\partial_t^2 - T_0\partial_x^2 + EI\partial_x^4 + 2\rho A\sigma_u^0\partial_t - 2\rho A\sigma_u^1\partial_t\partial_x^2\right) u(t,x) = \partial_x\left(g_u\psi\right) + \mathcal{J}f(t), \tag{65a}$$

$$\left(\rho A\partial_t^2 - T_0\partial_x^2 + 2\rho A\sigma_v^0\partial_t\right) v(t,x) = \partial_x\left(g_v\psi\right). \tag{65b}$$

(16c) and (17) hold here as well. This simplified loss model depends on three parameters $\sigma_u^0, \sigma_v^0, \sigma_u^1$, the latter of which controls a frequency dependent decay. The left-hand side of (65a) is a model of the linear stiff string with loss, used in many previous works, see e.g. [8] (Chapter 7). Here, $\mathcal{J}$ describes the spatial distribution of the source term. For simplicity, one can choose

$$\mathcal{J} = \delta(x - x_f), \tag{66}$$

where δ represents a Dirac delta function, and where $0 < x_f < L$ is the point of contact along the string where the source acts (not including the end points). The function $f = f(t)$ is the time evolution of the source term. A simple model for striking/plucking may be obtained by means of raised/half raised cosine [8], as

$$f(t) = \frac{F_s}{2}\left(1 - \cos(\zeta\pi(t - t_0))/t_s\right), \;\; t_0 \leq t \leq t_0 + t_s, \tag{67}$$

and $f(t) = 0$ elsewhere. The parameters F_s (in Newtons), t_s (in seconds) and $\zeta \in \{1, 2\}$ control, respectively, the maximum exerted force, the contact duration, and the source type (1 for pluck, 2 for strike).

System (65) maintains a notion of passivity, in that it is possible to obtain an energy balance of the kind

$$\frac{dH}{dt} = -2\rho A\mathcal{P}(t) + \partial_t u(t, x_f) f(t), \tag{68}$$

where the energy $H(t)$ has the form (14), and where

$$\mathcal{P}(t) = \sigma_u^0 \left\|\partial_t u\right\|^2 + \sigma_v^0 \left\|\partial_t v\right\|^2 + \sigma_u^1 \left\|\partial_t\partial_x u\right\|^2 \geq 0. \tag{69}$$

The time evolution of the energy (68) expresses the power balance of the string with loss and source. In particular, there is no autonomous production of energy within the system: power is dissipated according to $2\rho A\mathcal{P}(t)$, and injected according to $\partial_t u(t, x_f) f(t)$.

7.1. Discretisation

The Dirac delta function can be approximated here by a vector $\mathbf{J} = J_m$, $1 \leq m \leq N-1$, i.e. [8] (Chapter 5)

$$\mathcal{J} = \delta(x - x_f) \to \mathbf{J}, \tag{70}$$

where

$$J_{m_f} = (1-\alpha)/h, \;\; J_{m_f+1} = \alpha/h, \tag{71a}$$

Here $\alpha = x_f/h - m_f$, $m_f = \text{floor}(x_f/h)$. $\mathbf{J}$ is zero elsewhere. The loss terms are discretised simply as

$$\sigma_u^0 \partial_t - \sigma_u^1 \partial_t \partial_x^2 \to \sigma_u^0 \delta_{t\cdot} - \sigma_u^1 \delta_{t\cdot} \mathbf{D}^2, \quad \sigma_v^0 \partial_t \to \sigma_v^0 \delta_{t\cdot}. \tag{72}$$

The source is simply approximated as $f(t) \to f^n$, though one should be aware that formal order of accuracy may not be preserved under such choice [40]. This particular discretisation leads to passivity in the numerical setting. Via the same steps leading to (45) in the conservative case, one gets

$$\delta_{t+} \mathfrak{h}^{n-1/2} = -2\rho A \mathfrak{p}^n + \langle \mathbf{J}, \delta_{t\cdot} \mathbf{u}^n \rangle \, f^n, \tag{73}$$

where

$$\mathfrak{p} = \sigma_u^0 \left\| \delta_{t\cdot} \mathbf{u} \right\|^2 + \sigma_v^0 \left\| \delta_{t\cdot} \mathbf{v} \right\|^2 + \sigma_u^1 \left\| \mathbf{D}^- \delta_{t\cdot} \mathbf{u} \right\|^2 \geq 0. \tag{74}$$

Notice that stability condition (64) must be enforced here too.

7.2. Experiments

The performance of the discrete system is now checked in a number of numerical experiments. For those, the string's loss and source parameters are selected as in Table 4, while the other string parameters are the same as in Table 1.

Notice that three possible values for F_s can be selected from Table 4. Moreover, output is extracted at $x_o = 0.32$ m. For the simulations, a base sample rate $f_s = 48 \cdot 10^3$ Hz is used, and oversampling factors are indicated in the caption of the figures. For all the simulations, the grid spacing is chosen as $h = 1.05 h_0$, where h_0 is the limit of stability defined in (64): selecting the grid spacing slightly away from the limit of stability results in better numerical behaviour overall, as explained in the last paragraph of Section 5.1. Note that, in order to set θ_u in (62), one should employ a modified value

	units	value
σ_u^0	1/s	0.1
σ_v^0	1/s	0.2
σ_u^1	m^2/s	$4 \cdot 10^{-4}$
t_0	ms	1
t_s	ms	0.8
x_f	m	0.72
μ	-	2
F_s	N	[0.5,1,2]

Table 4: Loss and forcing parameters used for the time domain simulations, completing the parameters given in Table 1.

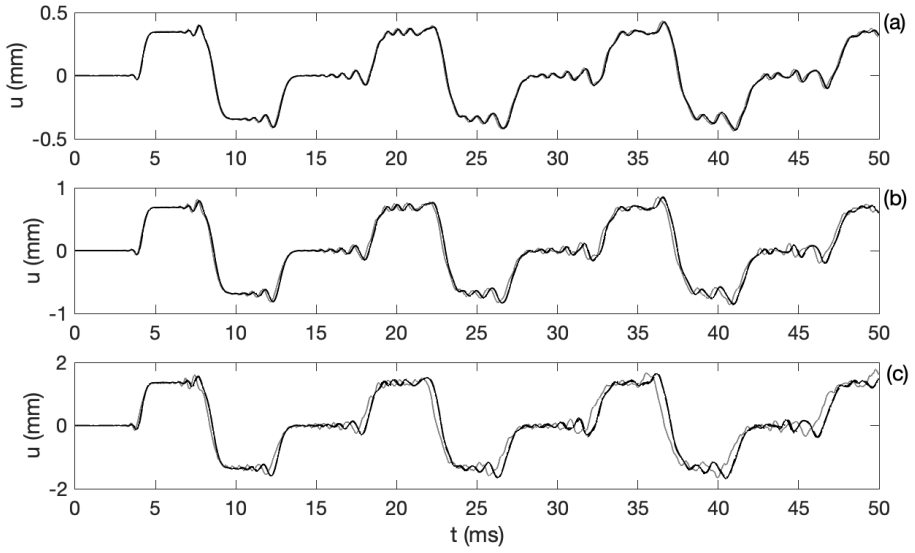

Figure 5: Transverse displacement. (a): $F_s = 0.5$ N; (b): $F_s = 1$ N; (c): $F_s = 2$ N. Oversampling factors: 1 (grey); 5 (solid black); 10 (dotted black); 15 (dashed black).

for $\bar{h}$, i.e. $\bar{h} = L/1.05N_u$. The number of longitudinal modes N_s is selected as per bound (50). A first experiment is presented in Figure 5. Here, the panels show the time evolution of the transverse waves for the three forcing values. The waveforms show that the wave velocity (and thus the frequency) increases with the forcing amplitude, a behaviour that is typical of nonlinear waves. In Figure 5(a), the dynamics is mostly linear, and one sees that

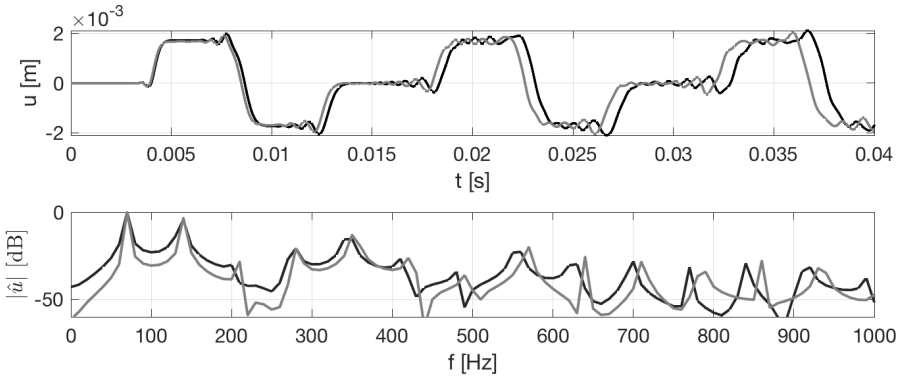

Figure 6: Longitudinal displacement. (a): $F_s = 0.5$ N; (b): $F_s = 1$ N; (c): $F_s = 2$ N. Oversampling factors: 1 (grey); 5 (solid black); 10 (dotted black); 15 (dashed black).

the solution computed at audio rate is virtually undistinguishable from the others. Indeed, in Figure 6(a) the solution computed at audio rate clearly drifts away from the others, but such effect is unperceivable when listening to the transverse component, see also the audio examples on the companion webpage[2]. As the forcing amplitude increases, as in panels (b) and (c) of Figure 5, the reference solution at audio rate diverges from the others, and

[2] https://mdphys.org/JSV_2022.html

higher oversampling factors may be needed (here, an oversampling factor of 5 seems to yield reasonable waveforms in all cases). The same conclusions can be drawn observing the longitudinal waves in Figure 6. While the solutions at

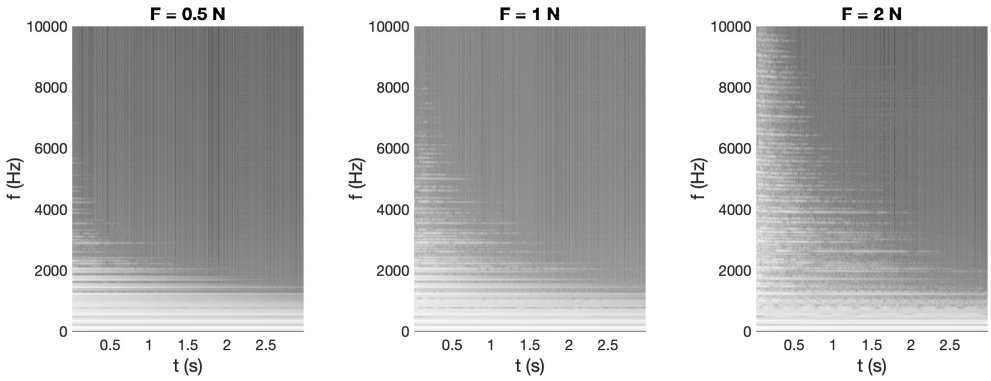

Figure 7: Velocity spectrograms for the three case studies. Input forcing amplitudes as indicated. The sample rate used is 48 kHz.

audio rate appear to not have converged at higher input forcings, they yield a perceptually reasonable sounding output, including pitch glides, phantom partials and modal couplings. These festures are visible in the spectrograms of Figure 7, highlighting the change from linear to nonlinear regimes. Sound examples, comparing the solutions obtained at audio rate with oversampled solutions, are available on the article's companion webpage[3].

8. Conclusions

String vibration is a subject of interest in many engineering disciplines. For the purpose of sound synthesis by physical modelling, as well as for advanced musical acoustics investigation, one must include nonlinear effects. These are distributed across the string, and arise as a consequence of the string's large stretching. In this work, an application of quadratisation methods was offered. This allows to solve for the nonlinearities using one single matrix inversion, thus bypassing the machinery of iterative methods. Longitudinal and transverse waves were solved using a mixed approach. The use of a free theta parameter allows to implement wideband numerical dispersion

[3] https://mdphys.org/JSV_2022.html

reduction in the transverse direction. Stability of the numerical scheme was approached via energy conservation, and illustrated numerically. Extension of these techniques to other nonlinearities in acoustics, such as collision dynamics [52, 53, 43, 33], von Kármán plates [8, 54], and others, is possible. Important aspects, worthy of future investigations, include a formal proof of convergence and accuracy, an analysis of structure of the scheme's matrices for improved performance, as well as the design of schemes with reduced dispersion in the longitudinal component.

Acknowledgements

The first author wishes to acknowledge the Leverhulme Trust, who supported this research with a Leverhulme Early Career Fellowship. This work was also supported by the European Research Council (ERC), under the European Union's Horizon 2020 research and innovation programme, grant 2020-StG-950084-NEMUS. The anonymous reviewers are also thanked for their comments and suggestions.

Appendix A. Error curves for the quadratised scheme

The simple case of a scalar nonlinear ODE is considered here, to check the order of accuracy of the proposed quadratised scheme. The scalar ODE reads

$$\frac{d^2u}{dt^2} = -u - \gamma u^3. \tag{A.1}$$

This is a type of lossless Duffing equation, with zero input. For this equation, an analytic solution exisits as

$$u(t) = u_0 \,\mathrm{cn}\left(\sqrt{1+\gamma u_0^2}\, t;\, \frac{\gamma u_0^2}{2\gamma u_0^2 + 2}\right), \tag{A.2}$$

where $\mathrm{cn}(a;b)$ is the Jacobi elliptic function with argument a and parameter b. Here, it is assumed that $u(t=0) = u_0$, $\frac{du(t=0)}{dt} = 0$. Numerical integration of (A.1) using the quadratised energy proceeds as follows. First, define the auxiliary variable

$$\psi = \sqrt{\frac{\gamma}{2}u^4} = \sqrt{\frac{\gamma}{2}}u^2. \tag{A.3}$$

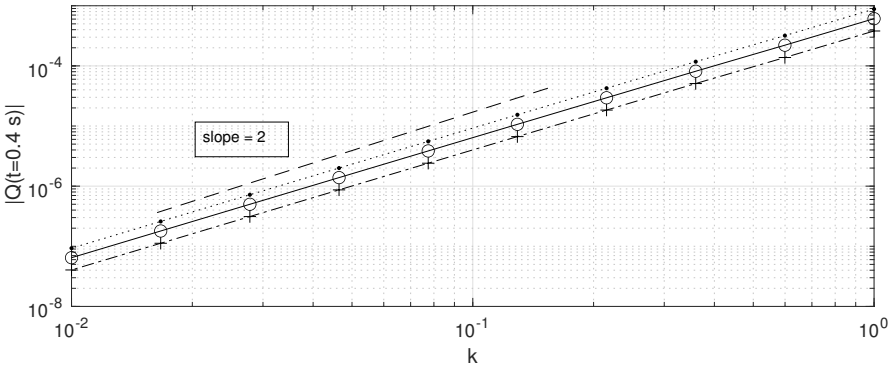

Figure A.8: Error curves of the quadratised scheme (A.4). Here, + is $\gamma = 0.6$, $\circ$ is $\gamma = 0.8$, $\cdot$ is $\gamma = 1$. The initial displacement is selected as $u_0 = 3.7$, and the error is computed at the time $t = 0.4$ s. The dashed line has a slope of 2.

The scheme is constructed as

$$\delta_{tt}u^n = -u^n - g^n\mu_{t+}\psi^{n-1/2},\ \delta_{t+}\psi^{n-1/2} = g^n\delta_{t\cdot}u^n,\ g^n = \frac{d\psi}{du}\Big|_{u=u^n}. \tag{A.4}$$

Numerical initial conditions are specified as

$$u^0 = u_0,\ u^1 = u^0 - \frac{k^2}{2}(u^0 + \gamma(u^0)^3),\ \psi^{1/2} = \sqrt{\frac{\gamma}{2}}(u^0)^2. \tag{A.5}$$

These are second-order accurate. Note, in particular, that u^1 was obtained implementing $\frac{d}{dt} = \delta_{t+} - \frac{k}{2}\delta_{tt} + O(k^2)$. The error at the time $t_e = \text{round}(0.4/k)k$ is then computed as

$$Q = u(t_e) - u^{t_e/k}, \tag{A.6}$$

that is, the difference between the analytic solution (A.2) and the output of the finite difference scheme at the corresponding time step. The error curves, under various choices of the nonlinear parameter γ, are plotted in Fig. A.8, and are second-order.

Appendix B. Error curves for the linear wave equation with stiffness

The linear part of (43a) is parametrised in terms of the switch $\eta \in \{0, 1\}$. When $\eta = 0$, the fourth-order differential operator is discretised explicitly.

As seen in Section 4.2, this leads to two different stability conditions for the two schemes. When the time step is selected as input parameter, and the schemes are run near the stability limits, the scheme with $\eta = 0$ is more efficient, since the corresponding grid spacing is larger. In terms of numerical dispersion, the scheme with $\eta = 0$ has better wideband behaviour, as seen in Figure 3. However, the scheme with $\eta = 0$ is only first-order convergent in time, since $k = O(h^2)$. The question that is addressed here is how formal first-order accuracy affects the space-time convergence. First, the space-time error is defined as

$$Q = u(t_e, x_e) - u_{x_e/h}^{t_e/k}, \tag{B.1}$$

where $t_e = kn$ is measured in seconds, $x_e = mh$ in meters, and $n \triangleq t_e/k$, $m \triangleq x_e/h$ are intergers. Furthermore, $u(t, x)$ denotes the true solution which, under simply-supported boundary conditions, reads

$$u(t, x) = \sum_{m=1}^{M} \left(C_m e^{j\Omega_m t} + C_m^\star e^{-j\Omega_m t} \right) \sin \frac{m\pi x}{L}. \tag{B.2}$$

Here, $C_m \in \mathbb{C}$ is a complex constant, with complex conjugate $C_m^\star$, to be determined from the initial conditions. M is, in theory, infinite, but for all practical puroposes it must be truncated to an integer (for the tests here, $M = 10^6$ is selected). The resonant frequencies are given by

$$\Omega_m = \sqrt{\frac{T_0}{\rho A} \left(\frac{m\pi}{L} \right)^2 + \frac{EI}{\rho A} \left(\frac{m\pi}{L} \right)^4}. \tag{B.3}$$

The initial displacement is selected as a raised cosine with compact support:

$$u(t = 0) \triangleq u_0(x) = \begin{cases} 1 - \cos\left(\frac{2\pi(x - L/4)}{L/2} \right) & \text{if } L/4 \leq x \leq 3L/4, \\ 0 & \text{elsewhere.} \end{cases} \tag{B.4}$$

The initial velocity is selected as $\frac{du(t=0)}{dt} = 0$. Under such initial conditions, the solution is

$$u(t, x) = \sum_{m=1}^{M} 2C_m \cos(\Omega_m t) \sin \frac{m\pi x}{L}, \tag{B.5}$$

with

$$C_m = \frac{\left\langle u_0, \sin \frac{m\pi x}{L} \right\rangle}{L}, \tag{B.6}$$

where the inner product is defined in (4). These integrals can be computed analytically, ultimately yielding an analytic expression for $u(t,x)$ for all times. The numerical schemes are initialised using

$$u_m^0 = u_0(x = mh), \tag{B.7a}$$

$$\mathbf{u}^1 = \mathbf{u}^0 + \frac{k^2}{2}\left(\frac{T_0}{\rho A}\mathbf{D}^2 - \frac{EI}{\rho A}\mathbf{D}^4\right)\mathbf{u}^0. \tag{B.7b}$$

These expressions for the initial conditions are second-order accurate. In particular, (B.7b) is obtained using the fact that $\frac{d}{dt} = \delta_{t+} - \frac{k}{2}\delta_{tt} + O(k^2)$. Then, a number N of subintervals is selected, with N even. The corresponding grid spacing h is obtained as $h = L/N$, and the time step is then selected by inverting (47) at the limit of stability, i.e.

$$k = \begin{cases} h^2\sqrt{\dfrac{\rho A}{T_0 h^2 + 4EI}}, & \text{if } \eta = 0, \qquad \text{(B.8a)} \\ \sqrt{\dfrac{\rho A}{T_0}}\,h, & \text{if } \eta = 1. \qquad \text{(B.8b)} \end{cases}$$

The error is computed at $x_e = L/2$, $t_e = \text{round}(10^{-3}/k)k$. Figure B.9 reports the error curves for a typical string, displaying the expected trends. Note that, when plotted against h, the errors are basically equal for both schemes: when $\eta = 0$, the corresponding time step k is much smaller at the limit of stability, allowing to compensate for the lower order of accuracy.

Appendix C. Error curves for the θ-schemes of the linear wave equation with stiffness

The order of accuracy of the parameterised scheme (59) is checked. From the stability condition (64), it is clear that the grid spacing h is not simply proportional to the time step k, as would be in a pure CFL condition. For this reason, the specification of the order of accuracy may be done in terms a new variable that parametrises uniquely the level curve $h - h_0(k, \theta_u) \approx 0$ in the (h,k) plane, where h_0 is as per (64). First, note that level curve can be expressed as

$$k = h^2\sqrt{\frac{\rho A(2\theta_u - 1)}{T_0 h^2 + 4EI}}. \tag{C.1}$$

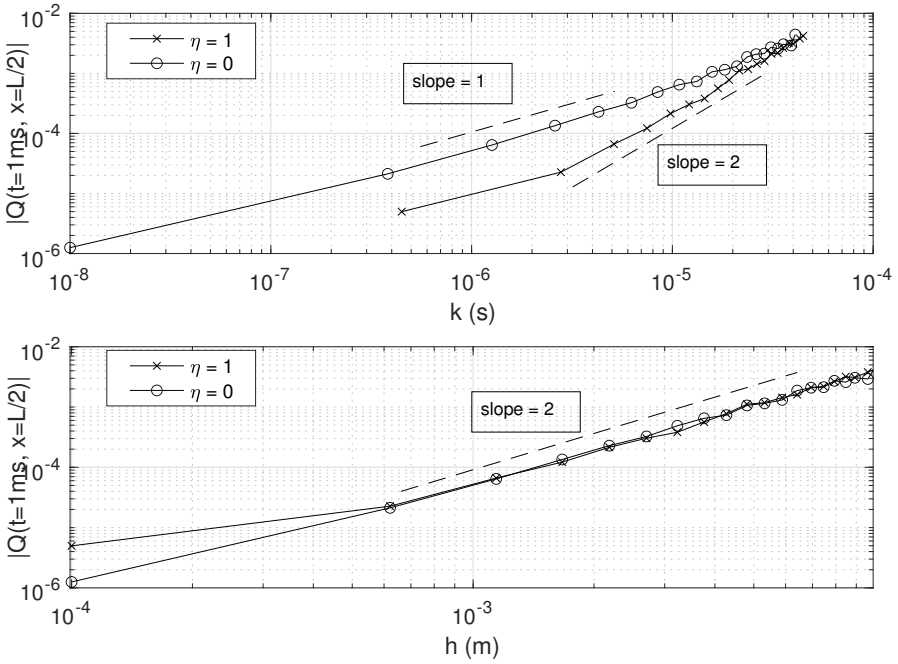

Figure B.9: Space-time errors of the schemes with $\eta = 0$ and $\eta = 1$, plotted against k and h. Here, the grid spacing is chosen as input parameter for the simulations, and the time step is selected at the corresponding limits of stability for the two schemes. A string with $\rho = 8000$ kg/m^3, $E = 2 \cdot 10^{11}$ Pa, $r = 0.2$ mm, $L = 1$ m, $T_0 = 50$ N was used for the simulations. The error is computed as per (B.1).

This curve is naturally parametrised by the arclength s, defined as

$$s = \int_0^h \sqrt{1 + \left(\frac{dk}{dh}\right)^2}\, \mathrm{d}h = h + \frac{\rho A(2\theta_u - 1)}{6EI} h^3 + O(h^5). \tag{C.2}$$

In Figure C.10, a check on the convergence of the numerical eigenfrequencies is performed. It is seen that clearly the errors are $O(s^2)$, for small enough s, and irrespective of the choice of θ_u (so long, of course, that $\theta_u > 1/2$, as specified at the end of Section 6). A second check is performed in the time domain. Here, the value of the numerical solution (at a given location along the grid, and at a given time) is compared against the analytic solution given in (B.5). The error has the same form as (B.1), and is computed at $x_e = L/2$, $t_e = \mathrm{round}(10^{-3}/k)k$. Again, the error curves display the expected error trends.

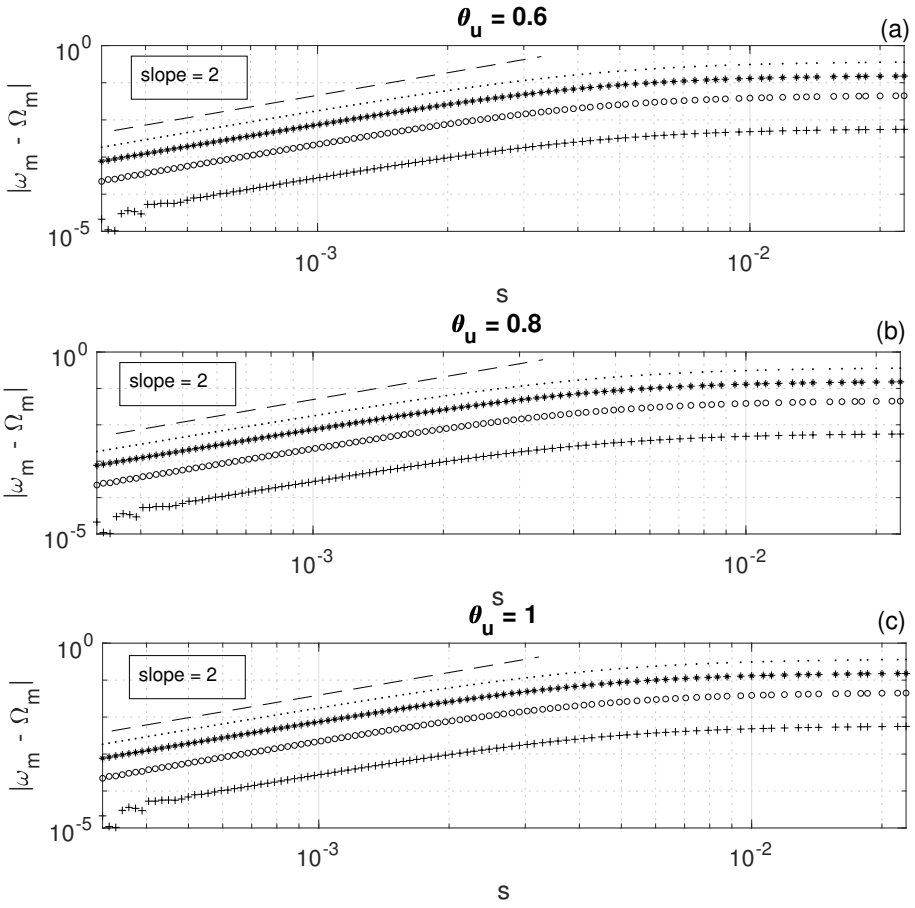

Figure C.10: Numerical errors of the first four eigenfrequencies of scheme (59), under various choices of θ_u, plotted against the arclength s. Here, the numerical eigenfrequencies ω_m are given by (63). The analytic eigefrequencies Ω_m are as per (B.3). For all panels, $+$ is $m = 1$, $\circ$ is $m = 2$, $*$ is $m = 3$, and $\cdot$ is $m = 4$. The superimposed dashed lines have a slope of 2. A string with $\rho = 8000$ kg/m^3, $E = 2 \cdot 10^{11}$ Pa, $r = 0.2$ mm, $L = 1$ m, $T_0 = 50$ N was used for the simulations.

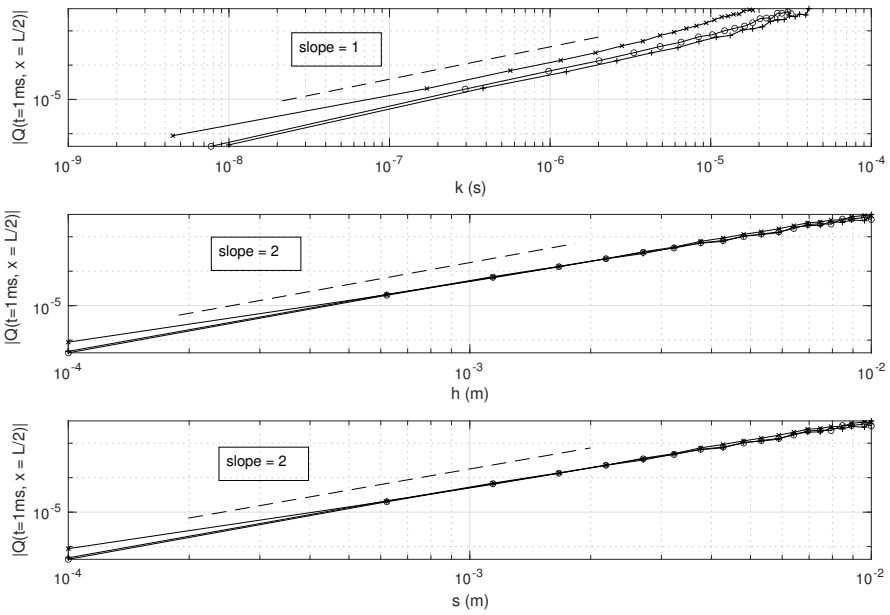

Figure C.11: Space-time error curves for scheme (59), under various choices of the parameter θ_u, and plotted against k, h and s. For all panels x is $\theta_u = 0.6$, $\circ$ is $\theta_u = 0.8$, and $+$ is $\theta_u = 1$. Dashed lines give the error slopes. A string with $\rho = 8000$ kg/m^3, $E = 2 \cdot 10^{11}$ Pa, $r = 0.2$ mm, $L = 1$ m, $T_0 = 50$ N was used for the simulations.

[1] P. Ruiz, A technique for simulating the vibrations of strings with a digital computer, Master's thesis, University of Illinois, 1969.

[2] L. Hiller, P. Ruiz, Synthesizing Musical Sounds by Solving the Wave Equation for Vibrating Objects: Part I, J Audio Eng Soc 19 (6) (1971) 462–470.

[3] R. Bacon, J. Bowsher, A discrete model for of the struck string, Acustica 41 (1978) 21–27.

[4] A. Chaigne, A. Askenfelt, Numerical simulations of piano strings 1. A physical model for a struck string using finite difference methods, J Acoust Soc Am 95 (2) (1994) 1112–1118.

[5] J. Bensa, S. Bilbao, R. Kronland-Martinet, J. O. Smith, The simulation of piano string vibration: From physical models to finite difference schemes and digital waveguides, J Acoust Soc Am 114 (2) (2003) 1095–1107.

[6] É. Ducasse, On waveguide modeling of stiff piano strings, J Acoust Soc Am 118 (3) (2005) 1776–1781.

[7] G. F. Carrier, On the non-linear vibration problem of the elastic string, Quart Appl Math 3 (2) (1945) 157–165.

[8] S. Bilbao, Numerical Sound Synthesis: Finite Difference Schemes and Simulation in Musical Acoustics, Wiley, Chichester, UK, 2009.

[9] T. Hélie, D. Roze, Sound synthesis of a nonlinear string using Volterra series, J Sound Vib 314 (1) (2008) 275–306.

[10] R. Narasimha, Non-Linear vibration of an elastic string, J Sound Vib 8 (1) (1968) 134–146.

[11] D. R. Rowland, The potential energy density in transverse string waves depends critically on longitudinal motion, Eur J Phys 32 (6) (2011) 1475–1484.

[12] P. Morse, U. Ingard, Theoretical Acoustics, Princeton University Press, Princeton, NJ, USA, 1968.

[13] S. Bilbao, Conservative numerical methods for nonlinear strings, J Acoust Soc Am 118 (5) (2005) 3316–3327.

[14] M. Ducceschi, S. Bilbao, Modelling Collisions of nonlinear strings against rigid barriers: Conservative Finite Difference Schemes With Application to Sound Synthesis, in: Proc. Int Conf Acous (ICA 2016), Buenos Aires, Argentina, 2016.

[15] B. Bank, L. Sujbert, Generation of longitudinal vibrations in piano strings: From physics to sound synthesis, J Acoust Soc Am 117 (4) (2005) 2268–2278.

[16] L. Ta-Tsien, Global classical solutions for quasilinear hyperbolic systems, Wiley, Michigan, USA, 1994.

[17] J. Chabassier, P. Joly, Energy preserving schemes for nonlinear Hamiltonian systems of wave equations: Application to the vibrating piano string, Comput Method Appl Mech 199 (45) (2010) 2779–2795.

[18] J. Chabassier, Modélisation et simulation numérique d'un piano par modèles physiques. (Modeling and simulation of a piano by physical modelling.), Ph.D. thesis, Ecole Polytechnique X, Paris, 2012.

[19] F. Marazzato, A. Ern, C. Mariotti, L. Monasse, An explicit pseudo-energy conserving time-integration scheme for Hamiltonian dynamics, Comput Method Appl Mech 347 (2019) 906 – 927.

[20] V. Chatziioannou, S. Schmutzhard, S. Bilbao, On Iterative Solutions for Numerical Collision Models, in: Proc Int Conf On Digital Audio Effects (DAFx-17), Edinburgh, UK, 2017.

[21] X. Yang, Linear, first and second-order, unconditionally energy stable numerical schemes for the phase field model of homopolymer blends, J Comput Phys 327 (2016) 294–316, ISSN 0021-9991.

[22] X. Yang, Linear and unconditionally energy stable schemes for the binary fluid-surfactant phase field model, Comp Methods Appl Mech Eng 318 (2017) 1005–1029.

[23] J. Zhao, Q. Wang, X. Yang, Numerical approximations for a phase field dendritic crystal growth model based on the invariant energy quadratization approach, Int J Numer Meth Eng 110 (3) (2017) 279–300.

[24] J. Chabassier, A. Chaigne, P. Joly, Modeling and simulation of a grand piano, J Acoust Soc Am 134 (1) (2013) 648–665.

[25] S. Han, H. Benaroya, T. Wei, Dynamics of transversely vibrating beams using four engineering theories, J Sound Vib 225 (3) (1999) 935–988.

[26] M. Ducceschi, S. Bilbao, Linear stiff string vibrations in musical acoustics: Assessment and comparison of models, J Acoust Soc Am 140 (4) (2016) 2445–2454.

[27] N. Lopes, T. Hélie, A. Falaize, Explicit second-order accurate method for the passive guaranteed simulation of port-Hamiltonian systems, in: Proc 5th IFAC 2015, Lyon, France, 2015.

[28] A. Falaize, Modélisation, simulation, génération de code et correction de systèmes multi-physiques audios: Approche par réseau de composants et formulation Hamiltonienne À Ports. (Modeling, Simulation, code generation and correction of multiphysics audio systems: Component network approach and Port-Hamiltonian formulation), Ph.D. thesis, Université Pierre et Marie Curie, Paris, 2016.

[29] A. Falaize, T. Hélie, Passive Guaranteed Simulation of Analog Audio Circuits: A Port-Hamiltonian Approach, Appl Sci 6 (2016) 273–273.

[30] N. Lopes, Approche passive pour la modélisation, la simulation et létude dun banc de test robotisé pour les instruments de type cuivre. (Passive approach for modelling, simulation and study of a robotic test bench for brass instruments.), Ph.D. thesis, Université Pierre et Marie Curie, Paris, 2016.

[31] C. Jiang., W. Cai, Y. Wang, A Linearly Implicit and Local Energy-Preserving Scheme for the Sine-Gordon Equation Based on the Invariant Energy Quadratization Approach, J Sci Comput 80 (2019) 1629–1655.

[32] M. Ducceschi, S. Bilbao, Non-iterative, conservative schemes for geometrically exact nonlinear string vibration, in: Proc Int Conf Acoust (ICA 2019), Aachen, Germany, 2019.

[33] M. Ducceschi, S. Bilbao, S. Willemsen, S. Serafin, Linearly-implicit schemes for collisions in musical acoustics based on energy quadratisation, J. Acoust. Soc. Am. 149 (5) (2021) 3502–3516.

[34] A. Torin, S. Bilbao, A 3D multi-plate environment for sound synthesis, in: Proc Int Conf On Dig Audio Eff (DAFx-13), Maynooth, Ireland, 2013.

[35] J. Gazdag, Numerical convective schemes based on accurate computation of space derivatives, J Comput Phys 13 (1) (1973) 100 – 113.

[36] J. Gazdag, Modeling of the acoustic wave equation with transform methods, Geophysics 46 (6) (1981) 854–859.

[37] M. Ducceschi, S. Bilbao, Conservative finite difference time domain schemes for the prestressed Timoshenko, shear and Euler-Bernoulli beam equations, Wave Motion 89 (2019) 142 – 165.

[38] R. LeVeque, Finite Difference Methods for Ordinary and Partial Differential Equations. Steady State and Time Dependent Problems, SIAM, Philadelphia, USA, 2007.

[39] P. Joly, Variational methods for time-dependent wave propagation problems, in: J. Fagerberg, D. C. Mowery, R. R. Nelson (Eds.), Topics in Computational Wave Propagation, Lecture Notes in Computational Science and Engineering, Springer, Berlin, 201–264, 2003.

[40] J. Chabassier, S. Imperiale, Space/time convergence analysis of a class of conservative schemes for linear wave equations, Comptes Rendus Mathematique 355 (3) (2017) 282–289.

[41] J. R. Bunch, J. E. Hopcroft, Triangular Factorization and Inversion by Fast Matrix Multiplication, Math Comput 28 (125) (1974) 231 – 236.

[42] T. Itoh, K. Abe, Hamiltonian-conserving discrete canonical equations based on variational difference quotients, J. Comput. Phys. 76 (1) (1988) 85–102.

[43] V. Chatziioannou, M. van Walstijn, Energy conserving schemes for the simulation of musical instrument contact dynamics, J Sound Vib 339 (2015) 262–279.

[44] G. Cohen, P. Joly, Construction analysis of fourth-order finite difference schemes for the acoustic wave equation in nonhomogeneous media, SIAM J Numer Anal 33 (4) (1996) 1266–1302.

[45] P. Joly, J. Rodríguez, Optimized higher order time discretization of second order hyperbolic problems: Construction and numerical study, J Comput Appl Math 234 (6) (2010) 1953–1961.

[46] M. Dablian, The application of high order differencing for the scalar wave equation, Geophysics 51 (1986) 54–56.

[47] R. Warming, B. Hyett, The modified equation approach to the stability and accuracy analysis of finite-difference methods, J Comput Phys 14 (2) (1974) 159–179.

[48] S. Bilbao, B. Hamilton, Higher-order accurate two-step finite difference schemes for the many-dimensional wave equation, J Comput Phys 367 (2018) 134–165.

[49] F. G. Germain, K. J. Werner, Design principles for lumped model discretisation using Moebius transforms, in: Proc Digital Audio Effects (DAFx-15), Trondheim, Norway, 2015.

[50] M. Ducceschi, S. Bilbao, C. Webb, Non-iterative Schemes For The Simulation Of Nonlinear Audio Circuits, in: Proc Digital Audio Effects (DAFx-21), Vienna, Austria, 2021.

[51] S. K. Lele, Compact finite difference schemes with spectral-like resolution, J Comput Phys 103 (1) (1992) 16–42.

[52] S. Bilbao, A. Torin, V. Chatziioannou, Numerical Modeling of Collisions in Musical Instruments, Acta Acust United with Acust 101 (2015) 155–173.

[53] M. Ducceschi, S. Bilbao, Non-iterative solvers for nonlinear problems: the case of collisions, in: Proc 22nd Conf of Digital Audio Effects (DAFx-19), Birmingham, UK, 2019.

[54] M. Ducceschi, O. Cadot, C. Touzé, S. Bilbao, Dynamics of the wave turbulence spectrum in vibrating plates: A numerical investigation using a conservative finite difference scheme, Physica D 280-281 (2014) 73–85.